Mechanisms for normal fault development at mid-ocean ridges

Mark D. Behn
MIT-WHOI Joint Program, Woods Hole, Massachusetts

Jian Lin
Department of Geology and Geophysics, Woods Hole Oceanographic Institution, Woods Hole, Massachusetts

Maria T. Zuber[1]
Department of Earth, Atmospheric and Planetary Sciences, Massachusetts Institute of Technology, Cambridge, Massachusetts

Short title: BEHN ET AL.: NORMAL FAULT DEVELOPMENT AT MID-OCEAN RIDGES

[1]Also at: Laboratory for Terrestrial Physics, NASA/Goddard Space Flight Center, Greenbelt, Maryland.

Abstract. Slow-spreading ridge segments are characterized not only by small, closely spaced faults that develop near the segment center, but also by large, widely spaced faults that develop near the segment ends, typically at the inside corner of a ridge-offset intersection. In this study we investigate the competing effects of stress accumulation in the lithosphere and the yield strength of the lithosphere in controlling the location of normal fault formation and direction of propagation. Seismic velocity models from the Mid-Atlantic Ridge in the Oceanographer-Hayes region and $29°$N and the East Pacific Rise at $9°$N were used to estimate the along-axis change in dynamic Young's modulus. Corresponding thermal and rheologic models were calculated to estimate the along-axis variation in yield strength. We then develop a thin-plate model to calculate the predicted location of fault initiation or reactivation and the subsequent propagation direction for different combinations of linear along-axis gradients in Young's modulus and yield strength. Based on this model we define two modes of normal fault development at slow-spreading segments: Mode C (Center) faults, which develop at the segment center and propagate outward, and Mode E (End) faults, which develop at the segment ends and propagate inward. Mode C faults are predicted to form at ridges where the along-axis variation in yield strength dominates the along-axis accumulation of stress. Conversely, Mode E faults are predicted to develop at ridges where stress accumulation toward segment ends overcomes the high yield strength in these locations. In addition to the accumulation of stress caused by along-axis gradients in Young's modulus, we illustrate that shear stresses resisting relative plate motion along a transform fault will generate higher effective stress at inside corners, possibly concentrating Mode E faulting in these locations. At fast-spreading ridges, where along-axis gradients in stress and lithospheric strength are relatively small, more uniform patterns of faulting are predicted. The results of this study quantify how the interplay between the along-axis variations in stress state and the mechanical properties of the lithosphere controls the style of fault development at mid-ocean ridge segments.

1. Introduction

The structure of oceanic crust formed at a ridge axis is controlled by the interplay between magmatic and tectonic processes. To first order, the relative importance of tectonic extension by faulting in seafloor spreading appears to increase with decreasing spreading rate [*Edwards et al.*, 1991; *Carbotte and Macdonald*, 1994; *Goff et al.*, 1997]. Furthermore, the style of tectonic faulting also varies with spreading rate. Faults formed at slow-spreading ridges are generally longer, with greater throw and larger spacing than faults formed at faster spreading rates [e.g., *Searle and Laughton*, 1981; *Macdonald*, 1982]. Systematic variations in faulting are also observed along individual segments of the slow-spreading Mid-Atlantic Ridge (MAR) [e.g., *Shaw*, 1992; *Shaw and Lin*, 1993; *Escartín et al.*, 1999]. Near segment centers, where negative residual gravity anomalies [e.g., *Kuo and Forsyth*, 1988; *Lin et al.*, 1990; *Detrick et al.*, 1995] and seismic velocity structure [e.g., *Tolstoy et al.*, 1993; *Hooft et al.*, 2000] indicate crustal thickness to be greatest, faults are observed to be linear, closely spaced, with relatively small throws. Toward segment offsets, however, faults become more oblique, fault spacing increases, and the amount of throw on an individual fault is observed to increase (see Figure 1) [e.g., *Shaw and Lin*, 1993; *Searle et al.*, 1998; *Escartín et al.*, 1999]. In Figure 2 we present a geologic map of the MAR segment at 25°10'N (Segment 6 of *Purdy et al.* [1990]) based on a combination of multi-beam bathymetry data [*Purdy et al.*, 1990; *Smith et al.*, 1995] and Towed Ocean Bottom Instrument (TOBI) side-scan sonar data [*Smith et al.*, 1995]. Fault throw was mapped along individual faults based on strike-perpendicular bathymetry profiles, spaced every 1 km. Stars mark the locations of maximum throw along those faults for which it was possible to confidently determine throw along the entire length of the fault scarp.

Figure 1.

Figure 2.

Malinverno and Cowie [1993] and *Shaw and Lin* [1996] attributed the first-order dependence of fault style on spreading rate to changes in the mechanical strength of the lithosphere caused by the difference in thermal state between fast- and slow-spreading ridges. Moreover, the observed change in fault throw and spacing along individual slow-spreading segments has been hypothesized to reflect segment scale variations in the strength of the brittle lithosphere [*Shaw*, 1992; *Shaw and Lin*, 1996]. Near segment centers, where warmer temperatures and thicker crust are predicted, yield strength calculations show lithospheric

strength to be significantly reduced relative to the segment ends [*Shaw and Lin*, 1996; *Hirth et al.*, 1998].

The symmetry of faulting is also observed to vary along individual slow-spreading segments. At the segment center faulting is generally symmetric across-axis, often with several inward dipping faults nested to form the median valley [e.g., *Macdonald*, 1982]. Toward the segment ends, however, the crust becomes highly asymmetric with large throw, widely-spaced faults concentrated on the elevated crust of the inside corner of a ridge-transform intersection, and smaller more closely-spaced faults at the outside corner [*Severinghaus and Macdonald*, 1988; *Tucholke and Lin*, 1994; *Allerton et al.*, 1995; *Escartín et al.*, 1999]. Many of the faults formed on inside-corner crust are observed to have their maximum throw at or near the segment end (Figure 2). This observation suggests that these faults have initiated, or are preferentially reactivated, in these locations rather than at the segment center.

These observations raise a fundamental question regarding the mechanics of faulting at mid-ocean ridges. Namely, if thicker crust and elevated temperatures indicate a weaker plate at segment centers, why are many faults observed to initiate, or preferentially reactivate, in the stronger lithosphere near segment ends, particularly on inside-corner crust? One potential explanation is that at certain times stress accumulation in the lithosphere is enhanced toward the segment ends. Such an along-axis gradient in stress could be achieved if stress is preferentially released near the segment center due to greater magmatic extension in these areas [*Karson and Winters*, 1992; *Gràcia et al.*, 1999], while continuing to accumulate at the segment ends. Alternatively, variations in the elastic properties of the lithosphere [e.g., *Campbell*, 1978] or the geometry of a ridge-transform intersection [e.g., *Phipps Morgan and Parmentier*, 1984; *Pollard and Aydin*, 1984; *Grindlay and Fox*, 1993] could generate higher stresses toward segment ends.

Here we present the results of a modeling study to quantify the competing effects of stress accumulation in the lithosphere and the mechanical strength of the brittle plate, in order to predict the style of normal fault development and propagation. We show that at fast-spreading ridges the lack of strong along-axis gradients in stress and lithospheric strength lead to relatively uniform fault patterns. In contrast, at slow-spreading segments significant along-axis variations in these two parameters generate a more complex pattern of faulting depending on the relative importance of stress and the mechanical properties of the plate. These and other predictions are

compared with observations, and the implications for different styles of fault development at fast- and slow-spreading ridges are discussed.

2. Rheology of a Mid-Ocean Ridge Spreading Segment

In order to understand how the state of stress and the mechanical strength of the lithosphere vary at a typical spreading segment, we first examine the constraints on these parameters at mid-ocean ridge spreading centers.

2.1. Young's Modulus and State of Stress

Stress accumulation in the lithosphere is influenced by the elastic properties of the brittle layer. Hooke's law dictates that stress in an elastic body is directly proportional to the strain applied on the body and the Young's modulus of material. Therefore, bodies with a greater Young's modulus will experience higher stress for a given strain than bodies with a lower modulus. Numerous laboratory studies have estimated the static elastic properties of rocks typically found on mid-ocean ridges [e.g., *Bass*, 1995, and refs. therein]. However, because laboratory experiments can only be performed on small rock samples, they are highly dependent on local heterogeneities in the sample. In order to avoid this problem, we take advantage of the fact that seismic velocity is a function of the elastic properties of the medium, and use P-wave velocity models to estimate the dynamic Young's modulus of the lithosphere [e.g., *Cheng and Johnston*, 1981; *Eissa and Kazi*, 1988]. The relationship between static and dynamic Young's modulus is somewhat complex, particularly at low confining pressures. However, laboratory and in-situ studies have found that in general the ratio of static to dynamic Young's modulus is between 1 and 2 [*Eissa and Kazi*, 1988; *Gudmundsson*, 1988; *Forslund and Gudmundsson*, 1991].

Rewriting the equation for P-wave velocity gives the following expression for dynamic Young's modulus [*Jaeger and Cook*, 1979]

$$\mathrm{E} = \frac{\mathrm{v_p^2}\,(1+\nu)\,(1-2\nu)\,\rho}{(1-\nu)}, \tag{1}$$

where $\mathrm{v_p^2}$ is the P-wave velocity, ν is the Poisson's ratio, and ρ is the density. Applying Equation

1 to the P-wave velocity model of *Canales et al.* [2000b] for the western rift mountains of MAR segment OH-1 ($35°$N), we calculated a corresponding Young's modulus model (Figure 3). The crustal and mantle densities were taken from the model of *Canales et al.* [2000b], which is based on the velocity-to-density relationships of *Horen et al.* [1996] and *Miller and Christensen* [1997] and constrained by the observed gravity. Estimates of Poisson's ratio in oceanic crust range from 0.25–0.32 [e.g., *Christensen and Smewing*, 1981; *Bratt and Solomon*, 1984; *Collier and Singh*, 1998]. We choose an average value of 0.30 for Poisson's ratio and assign an uncertainty of $\pm$15% to our calculations of Young's modulus.

Figure 3.

In order to incorporate the observed variations in Young's modulus into a thin-plate model of a ridge segment, we assume that at any point the plate behaves in relation to the depth-averaged value of its rheologic properties. The dashed line in Figure 4a illustrates Young's modulus averaged to a depth of 8 km, which is the maximum depth of reasonable seismic resolution, along the *Canales et al.* [2000b] profile shown in Figure 3b. The depth-averaged value of Young's modulus increases from segment center toward the distal ends with an approximate gradient of 0.15–0.25 GPa/km, and then decreases by $\sim$10 GPa within the offsets bounding the segment to the north and south. We performed a similar calculation along the axis of segment OH-1 using the P-wave velocity model of *Hooft et al.* [2000] (solid line in Figure 4a). This calculation suggests that while the along-axis gradient in depth-averaged Young's modulus is similar both on- and off-axis, the off-axis profile is shifted to higher moduli by a constant value of 5–8 GPa. This would predict an across-axis gradient in Young's modulus of $\sim$0.15 GPa/km.

Figure 4.

We also calculated depth-averaged Young's modulus along the MAR segment at $29°$N (Figure 4d) and the EPR segment at $9°$N (Figure 4g) using the seismic velocity models of *Wolfe et al.* [1995] and *Canales et al.* [2001], respectively. The $29°$N segment of the MAR shows a similar gradient to that of the OH-1 segment, while the EPR segment shows little along-axis variation in Young's modulus outside the fracture zone and overlapping spreading center at the segment ends. These results imply that the increase in depth-averaged Young's modulus toward the ends of a slow-spreading segment is caused by thinner crust in these locations, resulting in a greater portion of the brittle plate to be composed of high Young's modulus mantle rocks, such as olivine and pyroxene. In contrast, at fast-spreading ridges the observed variations are much

smaller except locally near major ridge offsets.

An alternative approach is to average Young's modulus to the depth of the brittle-ductile transition, as opposed to a constant depth along the entire segment. The effect of this calculation would be to average to greater depths at the segment ends where the brittle-ductile transition is deeper (see Figure 3c), incorporating more high Young's modulus rocks of the lower crust and mantle and increasing the along-axis gradient. This approach was used along the OH-1 segment, and the resulting gradient was calculated to be $\sim$0.5 GPa/km, approximately twice the value calculated when averaging to a constant depth of 8 km. Thus, it is possible that the depth-averaged values shown in Figures 4a, 4d, and 4g underestimate the true along-axis gradients in Young's modulus.

2.2. Yield Strength

The mechanical strength of the lithosphere is often modeled using a strength-versus-depth profile ("yield strength envelope"), in which strength in the shallow, brittle regime is controlled by a frictional resistance law [e.g., *Byerlee*, 1978], while strength in the deeper, ductile regime is limited by power law creep [e.g., *Goetze and Evans*, 1979; *Brace and Kohlstedt*, 1980] (Figure 5).

Figure 5.

Depth-averaged yield strength was calculated along the OH-1, MAR $29°$N, and EPR $9°$N segments. Using the technique of *Phipps Morgan and Forsyth* [1988], we consider conductive and advective heat transfer in mantle flow driven solely by separating surface plates. Thermal models were calculated for each of the three spreading segments based on the appropriate spreading rate and ridge-offset geometry. Along each of the available seismic lines, strength-versus-depth profiles were computed (e.g., Figure 3c) and averaged to a depth of 15 km, below which changes are negligible. The resulting depth-averaged yield strengths for the three segments are shown in Figure 4. Because a constant coefficient of friction, $\mu = 0.85$, was used in all calculations, the along-axis gradients in depth-averaged yield strength are primarily thermally controlled.

Due to the thermal cooling effect of ridge offsets, along-axis changes in depth-averaged yield strength are highly dependent on the length of the bounding offset. At MAR $29°$N, for example, where the offsets at either end of the segment are approximately 15 km in length, the

predicted along-axis gradient in yield strength is ∼0.3 MPa/km. In contrast, at the MAR OH-1 segment, where the northern end of the segment is bounded by the 100 km Oceanographer fracture zone, the predicted along-axis gradient in yield strength is >2.0 MPa/km. The along-axis variation in yield strength is also strongly dependent on spreading rate, with higher rates having smaller along-axis changes. Note that even though the southern end of the EPR 9°N segment is bounded by the 75 km long Siqueiros fracture zone, the depth-averaged yield strength remains relatively constant up to distances of <10 km from the offset.

The *Phipps Morgan and Forsyth* [1988] model neglects the effects of hydrothermal cooling in the shallow crust and the heat of magma emplacement at the ridge axis, which were considered in the models of *Shaw and Lin* [1996] (Figure 5a). Hydrothermal circulation preferentially cools those portions of the lithosphere where open cracks permit fluid flow beneath the seafloor. *Shaw and Lin* [1996] suggest this process would be enhanced toward segment ends, intensifying the cooling effect of ridge offsets, and further increasing the mechanical strength of the lithosphere in these locations (Figure 5d). Magma injection, on the other hand, would tend to increase temperatures near the center of a slow-spreading segment, where gravity and seismic models suggest greater crustal emplacement. This would decrease the mechanical strength of the lithosphere at the segment center (Figure 5b), and when combined with the effect of hydrothermal cooling, lead to stronger along-axis gradients in depth-averaged yield strength. We compare depth-averaged yield strength calculated at the center and end of a 50-km-long northern MAR segment using the *Phipps Morgan and Forsyth* [1988] and *Shaw and Lin* [1996] models. The results suggest that the addition of hydrothermal cooling and the heat of magma emplacement, as included in the *Shaw and Lin* [1996] model, may increase the along-axis gradient in yield strength by ∼50%.

In contrast, the effect of serpentinization may partially offset these effects. Serpentinized peridotites are observed to outcrop preferentially toward the end of slow-spreading segments, in particular at the inside corner of a ridge-offset intersection [*Karson et al.*, 1987; *Tucholke and Lin*, 1994; *Cannat et al.*, 1995]. *Escartín et al.* [1997] observed that serpentinites have a low coefficient of friction, $\mu \sim 0.3$, and thus can reduce the integrated strength of the lithosphere up to 30% toward the segment ends (Figure 5d). Therefore, if the coefficient of friction decreases from the center to the ends of a spreading segment due to the effects of serpentinites, it may

reduce the along-axis gradient in yield strength.

In summary, our calculations indicate that the along-axis gradients in depth-averaged Young's modulus and yield strength are in the range of 0.15–0.5 GPa/km and 0.2–2.5 MPa/km, respectively, along the slow-spreading MAR. In contrast, at the fast-spreading EPR, there appears to be little variation in either of these two parameters along a spreading segment, with the possible exception of a narrow (5–10 km) zone adjacent to a major offset. Due to the uncertainties involved, we use these estimates only as qualitative limits on the variations along an individual spreading segment. We then parameterize a thin-plate deformation model using linear gradients in Young's modulus and yield strength from the segment center to the distal ends.

3. Model Setup

To date most studies of faulting at mid-ocean ridges have focused on deformation in cross-sections through the lithosphere [e.g., *Tapponnier and Francheteau*, 1978; *Phipps Morgan et al.*, 1987; *Chen and Morgan*, 1990; *Lin and Parmentier*, 1990; *Shaw and Lin*, 1996; *Buck and Poliakov*, 1998; *Poliakov and Buck*, 1998]. However, in this study we attempt to quantify the spatial pattern of normal fault development along a ridge segment. We construct a thin-plate model for a single ridge segment. A plane stress approximation is adopted, in which the vertical tectonic stresses are assumed to be negligible relative to the horizontal stresses in the lithosphere and there is no stress coupling between the lithosphere and its underlying ductile asthenosphere. As illustrated in Figure 4, both the depth-averaged Young's modulus and yield strength are expected to vary along mid-ocean ridge segments, with the gradient a function of spreading rate and other factors. To parameterize the observed increase in Young's modulus, E, and yield strength, σ_{yield}, from segment center to the distal ends, we impose linear gradients in these two parameters (dE/dy and $\mathrm{d}\sigma_{\mathrm{yield}}/\mathrm{dy}$, respectively) along the ridge axis (Figures 6b and 6c). We also impose an across-axis gradient in yield strength ($\mathrm{d}\sigma_{\mathrm{yield}}/\mathrm{dx}$) twice the magnitude of the along-axis gradient in order to account for the thermal thickening of the lithosphere with age [e.g., *Watts et al.*, 1980] (see Table 1 for complete list of model parameters). Although Figure 4a suggests that an across-axis gradient in Young's modulus may be present at a typical

slow-spreading ridge segment, our calculations show that this gradient does not significantly influence the results of our model (see Appendix for complete discussion), and thus we assume Young's modulus to be constant in the across-axis direction (Figure 6b).

Figure 6.

Table 1.

A gradually increasing extensional strain is applied at far-field model boundaries (left and right) to simulate spreading and the resulting stresses are calculated analytically throughout the model domain (see Appendix). The far-field strain, $\varepsilon_{\mathrm{x}}^{\mathrm{f.f.}}$, is increased until the effective stress in the plate, defined as $\sigma_{\mathrm{eff}} = \left(\frac{1}{2}\left(\sigma_{\mathrm{x}}^2 + \sigma_{\mathrm{y}}^2 + \left(\sigma_{\mathrm{x}} - \sigma_{\mathrm{y}}\right)^2 + 6\tau_{\mathrm{xy}}^2\right)\right)^{1/2}$, exceeds the material yield stress at some location in the model domain. Once yielding occurs the elastic-plastic finite element model, ADINA [*Bathe*, 1996], is used to calculate the stresses and strains numerically throughout the model domain. We assume that after yielding the plate behaves as a perfectly plastic material, and the evolution of the plastic yield zone is examined to provide a qualitative description of the resulting region of normal faulting at the ridge axis.

4. Model Results

As the far-field extensional strain increases, stress will accumulate throughout the model space, until the effective stress exceeds the yield stress and failure occurs. Because the yield strength increases off-axis, initial failure is expected to occur at a point along the ridge axis. Due to the higher Young's modulus toward the segment ends, stress builds up more rapidly in these regions under elastic extension of the plate. Competing with this stress accumulation pattern is the positive gradient in yield strength from segment center to the distal ends, which favors yielding to occur first at the segment center where the yield strength of the plate is minimum.

Based on this model we define two modes of fault development at ridge segments: faults that develop at the segment center and propagate outward, called Mode C (Center) faults (Figures 7a and 7c), and faults that develop at the segment ends and propagate inward, called Mode E (End) faults (Figures 7b and 7d). Mode C faults are expected to form at ridges where the along-axis variation in yield strength dominates the along-axis accumulation of stress. Conversely, Mode E faults are expected to develop in environments where the stress accumulation associated with the along-axis gradient in Young's modulus overcomes the variation in yield strength (Figures 7b and 7d). Therefore, in our linear model it is the interplay between dE/dy and dσ_{yield}/dy

that determines whether failure is preferred at the segment center (Figures 7a and 7c) or at the segment ends (Figures 7b and 7d). Figure 8 shows calculation results illustrating how the relationship between dE/dy and $d\sigma_{yield}/dy$ controls the transition from Mode C to Mode E faults. The values for Young's modulus and yield strength at the segment center (E° = 75 GPa and σ°_{yield} = 50 MPa) are based on the depth-averaged Young's modulus and yield strength from the MAR OH-1 segment (Figures 4a and 4c).

Figure 7.

The relation between dE/dy and $d\sigma_{yield}/dy$ also plays an important role in controlling the evolution of the plastic yield zone after failure (Figure 9). In the case where enhanced accumulation of stress toward the segment ends perfectly balances the along-axis gradient in yield strength, the plate will break uniformly along the entire ridge axis (Figure 9c). However as dE/dy increasingly dominates $d\sigma_{yield}/dy$, the plastic zone associated with Mode E faults becomes more triangular in shape, and propagates less toward the segment center for a given value of $\varepsilon_x^{f.f.}$ (Figures 9a and 9b). In contrast, as $d\sigma_{yield}/dy$ is increased relative to dE/dy, it becomes increasingly difficult for Mode C faults to propagate outward toward the segment ends (Figures 9d and 9e).

Figure 8.

Figure 9.

Another interesting prediction of this model is that the calculated plastic zone related to Mode E faults is significantly wider in across-axis dimension than the plastic zone associated with Mode C faults. This calculation suggests that Mode E faults would tend to initiate and remain active over a broader across-axis region than Mode C faults. Several segments of the slow-spreading MAR have been documented to exhibit hour-glass shaped rift valleys [e.g., *Sempéré et al.*, 1993; *Detrick et al.*, 1995; *Weiland et al.*, 1996]. Although there is little geologic evidence constraining the width of the zone of fault initiation at ridge segments, *Bohnenstiehl and Kleinrock* [1999] used estimates of the amount of strain on individual faults to conclude that fault initiation is primarily confined within the median valley of a slow-spreading segment. If correct, this observation suggests that segments with hour-glass shaped rift valleys may be characterized by wider zones of fault initiation at the segment ends than at the center. Furthermore, *Shaw* [1992] and *Shaw and Lin* [1993] observed that faults near segment ends are typically characterized by greater amounts of throw than faults at segment centers. This observation could be explained if Mode E faults remain active, continuing to accumulate slip for a longer time period than Mode C faults.

The results of our model are moderately sensitive to the base values chosen for Young's modulus, E°, and yield strength, $\sigma^{\circ}_{\mathrm{yield}}$, at the segment center. The observed variations in these parameters with spreading rate and offset length (Figure 4) suggest the need to test the importance of E° and $\sigma^{\circ}_{\mathrm{yield}}$ in influencing the transition from Mode C to Mode E faults. Figure 10 shows the Mode C-E transition in dE/dy versus $d\sigma_{\mathrm{yield}}/dy$ phase space for four different combinations of E° and $\sigma^{\circ}_{\mathrm{yield}}$. Note that as $\sigma^{\circ}_{\mathrm{yield}}$ is decreased relative to E°, the slope of the Mode C-E transition increases and the region of phase space for Mode E faults decreases. In addition, the amount of far-field extensional strain required for initial yielding increases with increasing $\sigma^{\circ}_{\mathrm{yield}}$ and decreasing E°. **Figure 10.**

5. Discussion

5.1. Observations of Mode E Faults

At slow-spreading ridges new normal faults typically initiate within the rift valley where the lithosphere is thinnest [*Searle*, 1984; *Bicknell et al.*, 1987; *Carbotte and Macdonald*, 1990]. Once formed, these faults grow in the along-axis direction through a combination of lateral propagation and linkage with other faults [e.g., *Cowie*, 1998], while simultaneously being rafted off-axis due to the injection of dikes at the ridge axis. The point of maximum throw on a fault scarp represents the location at which the fault is preferentially reactivated over time, by slip events of higher frequency or larger magnitude. Several authors have argued that the location of maximum throw can be used as a proxy for the point of fault initiation [*Barnett et al.*, 1987; *Walsh and Watterson*, 1987]. If correct, this implies that many of the large faults observed toward the end of slow-spreading segments may not only accumulate slip preferentially in these locations, but may also initiate at or near the segment ends.

Figure 1a illustrates an excellent example of a large Mode E fault on inside-corner crust of the MAR OH-1 segment (oriented N45°E from 35°N to 35°10'N), with maximum throw near the segment end and tapering toward the segment center. Similarly, a series of discrete Mode E faults (oriented N45°E just south of 34°N) can be seen on the inside corner crust of segment OH-3 (Figure 1b). Another MAR segment that displays several prominent Mode E faults is at 25°10'N (Figure 2). Here faults are observed to accumulate maximum slip at different locations

along the segment, not only at the center and ends, but also in between. However, toward the ends of the segment large faults appears to be preferred on inside-corner crust. Other examples of Mode E faults have been documented elsewhere along the MAR [*Smith et al.*, 1995; *Searle et al.*, 1998; *Escartín et al.*, 1999; *Briais et al.*, 2000].

5.2. Factors Favoring the Generation of Mode E Faults

Figures 8 and 10 show the conditions under which along-axis changes in Young's modulus can generate large enough gradients in stress to overcome the increased lithospheric strength of the segment ends, thus forming Mode E faults. We note that the observed values of dE/dy along the MAR OH-1 and MAR 29°N segments are insufficient to generate the stress gradients necessary to produce the observed Mode E faults in these locations (Figure 8). Figure 11 shows the additional gradient in effective stress that is required to switch from Mode C to Mode E faulting as a function of dE/dy and dσ_{yield}/dy. Note that the closer a segment plots to the Mode C-E transition in Figure 11, the smaller the additional along-axis gradient in stress that is necessary to switch from one mode of faulting to the other.

Figure 11.

However, changes in Young's modulus are not the only source of along-axis variations in stress at a ridge segment. Furthermore, segments are rarely characterized by just one mode of faulting, as would be predicted if variations in dE/dy and dσ_{yield}/dy were the only parameters controlling fault development at a ridge segment. This observation suggests that temporal variations in stress must also play an important role in the dynamics of faulting at mid-ocean ridges. Below we discuss several mechanisms that may lead to the development of Mode E faults at a ridge segment.

5.2.1. Serpentinization One hypothesis that has been proposed to explain the generation of Mode E faults is that serpentinites may be sufficiently abundant toward the end of slow-spreading segments to significantly reduce the strength of the lithosphere in these locations [*Escartín et al.*, 1997]. If serpentinites are present in large enough quantities to offset the gradient in lithospheric strength caused by the change in thermal and crustal structure along a segment, it could explain the formation of Mode E faults at many ridge segments. At present, however, there are not sufficient observations to assess whether the effect of serpentinization alone is sufficient to offset the gradient in yield strength due to along-axis variations in thermal

and crustal structure. Further, the serpentinization model also has difficulty explaining the asymmetry observed at inside- and outside-corners.

5.2.2. Transform Fault Shearing An alternative mechanism that may increase stresses toward the end of a spreading segment is the effect of shear stress resisting relative plate motion along a transform fault. *Phipps Morgan and Parmentier* [1984] and *Grindlay and Fox* [1993] modeled the stress field associated with transform offsets by applying varying ratios of the tensile stress resisting plate separation at the ridge axis, σ_{R}, and the shear stress resisting relative plate motion along the offset, σ_{T}. The tensile stresses predicted by these models are amplified at the inside corners, with their magnitude increasing with greater offset lengths and smaller $\sigma_{\mathrm{R}}/\sigma_{\mathrm{T}}$ ratios. *Pollard and Aydin* [1984] predict a similar increase in stress at an inside corner without imposing any shear stress along the transform boundary, by modeling the propagation of two over-lapping cracks in an elastic plate.

Figure 12 illustrates the effect of imposing a shear stress resisting relative plate motion along a 30-km section of the top and bottom boundaries of the model space adjacent to the ridge axis. Assuming $\sigma_{\mathrm{R}} = \sigma^{\circ}_{\mathrm{yield}}$, we vary σ_{T} to show the change in effective stress associated with $\sigma_{\mathrm{R}}/\sigma_{\mathrm{T}}$ ratios of 2, 3, and 5 (Figures 12b, 12c, and 12d, respectively). Although for numerical simplicity we choose to vary only σ_{T}, we note that changes in σ_{R} may also affect the $\sigma_{\mathrm{R}}/\sigma_{\mathrm{T}}$ ratio. With the minor exception of a small region surrounding the point at which the ridge and transform meet, the inside corners are characterized by increased effective stresses relative to the outside-corners. The predicted $\mathrm{d}\sigma_{\mathrm{eff}}/\mathrm{dy}$ are up to $\sim$0.3 MPa/km at a distance of 15 km from the ridge axis. These values are comparable in magnitude to the predicted stress changes associated with along-axis variations in Young's modulus.

Figure 12.

Based on the observed rotation of normal fault scarps near non-transform offsets, *Grindlay and Fox* [1993] hypothesized that the $\sigma_{\mathrm{R}}/\sigma_{\mathrm{T}}$ ratio will generally fall in the range of 3 to 5. However, along segments characterized by low residual gravity and shallow axial bathymetry, the observed morphology was found to be more closely matched by a $\sigma_{\mathrm{R}}/\sigma_{\mathrm{T}}$ ratio of 1 to 3. *Grindlay and Fox* [1993] proposed that the decrease in $\sigma_{\mathrm{R}}/\sigma_{\mathrm{T}}$ might be caused by a reduction in σ_{R} related to periods of robust magmatic activity. If correct, this could indicate a link between enhanced magmatism at the segment center and increased tectonism at the inside corners.

This prediction is consistent with observations from the MAR OH-1 and OH-3 segments.

Residual gravity anomalies [*Detrick et al.*, 1995] and seismic refraction profiles [*Hooft et al.*, 2000; *Canales et al.*, 2000b] show the OH-1 segment to be magmatically robust, with young, sheet-like lava flows covering the axial valley floor at the segment center [*Gràcia et al.*, 1999]. Toward the segment ends the valley floor shows extensive faulting and fissuring, and a large Mode E fault is observed at the northeast inside corner (Figure 1a). In contrast, the OH-3 segment is characterized by a weaker, less stable magma source, offset to the south of the segment center [*Gràcia et al.*, 1999]. At OH-3 a series of small Mode E faults is observed at the inside corners, while the zone of most intense faulting and fissuring is near the segment center (Figure 1b). Note that while the calculated asymmetry in stresses between the inside and outside corners depends on the assumed $\sigma_{\mathrm{R}}/\sigma_{\mathrm{T}}$ ratio, the predicted stresses are always higher at the inside-corner crust than at the outside-corner and segment center. Thus transform shearing enhances the probability of forming Mode E faults on inside-corner crust.

5.2.3. Temporal Variations in Stresses Episodic periods of enhanced magmatic activity have been inferred from off-axis residual gravity anomalies on time scales of 2–5 m.y. [*Pariso et al.*, 1995; *Tucholke et al.*, 1997]. Moreover, a recent across-axis seismic profile at the MARK Area of the MAR suggested even shorter fluctuations in magma supply, with periods of 400–800 k.y. [*Canales et al.*, 2000a]. Thermal and crustal structure are critical in the determination of dE/dy and $\mathrm{d}\sigma_{\mathrm{yield}}/\mathrm{dy}$, and have been shown to vary as a function of magma supply [e.g., *Tucholke et al.*, 1997; *Canales et al.*, 2000a]. Thus, temporal variations in magmatic accretion at slow-spreading ridge axes may influence not only the ridge-transform coupling ratio $\sigma_{\mathrm{R}}/\sigma_{\mathrm{T}}$ as discussed above, but also the elastic and mechanical properties of the lithosphere.

In addition to variations due to magma supply, the process of faulting itself affects the local stress field. Stress drops associated with large earthquakes range from 1 to 10 MPa [*Kanamori and Anderson*, 1975]. A normal fault releases stress to either side of its center, but concentrate stress at its tips [e.g., *Pollard and Aydin*, 1984; *Crider and Pollard*, 1998]. As a population of normal faults evolves, the stress fields associated with individual faults interact, leading to the coalescence of multiple small faults into a few larger structures [e.g., *Cowie et al.*, 1993; *Tuckwell et al.*, 1998]. As this process continues, extension due to the linkage of existing faults will eventually begin to dominate over the nucleation of new faults [*Spyropoulos et al.*, 1999; *Ackermann and Schlische*, 1999]. These complications are beyond the scope of this study, but

illustrate that the stress field at a mid-ocean ridge segment changes constantly as new faults form and deformation continues on existing fault planes.

In summary, we suggest that along-axis variations in Young's modulus, shear stresses along a transform fault, and temporal variations in magma supply and fault growth can all lead to enhanced stresses toward the end of a segment. While any of these factors alone may be insufficient to generate a Mode E fault, together they can produce large enough stresses at the segment ends to overcome the positive along-axis gradient in yield strength.

5.3. Fault Initiation at Fast-Spreading Ridges

At slow-spreading MAR segments, variations in thermal and crustal structure cause dE/dy and $d\sigma_{yield}/dy$ to change significantly along-axis. In contrast, at the fast-spreading EPR Young's modulus and yield strength are observed to remain relatively constant along-axis (Figure 4). The lack of along-axis gradients in dE/dy and $d\sigma_{yield}/dy$ at the EPR would tend to favor uniform failure along the ridge axis, rather than the development of prominent Mode C or E faults. This prediction is consistent with observations of faulting at the EPR, which show numerous small, closely-spaced faults forming continuously along the entire spreading segment [e.g., *Carbotte and Macdonald*, 1994; *Alexander and Macdonald*, 1996].

6. Conclusions

In this study we present a thin-plate model of a ridge segment to examine the relative importance of lateral changes in stress accumulation and the mechanical strength of the brittle lithosphere at a mid-ocean ridge spreading center. Thermal and seismic velocity models along the MAR OH-1 and MAR $29°$N segments show that both Young's modulus and yield strength are expected to change considerably along a slow-spreading segment, while little variation in these parameters is observed at the fast-spreading EPR $9°$N segment. Higher values of depth-averaged Young's modulus toward the segment ends are calculated to lead to enhanced stress accumulation in these regions. Competing with this accumulation of stress is a positive gradient in yield strength from segment center to segment ends.

Based on this model we define two modes of fault development at slow-spreading segments:

Mode C (Center) faults, which develop at the segment center and propagate outward, and Mode E (End) faults, which develop at the segment ends and propagate inward. Mode C faults are predicted to form in ridge environments where the along-axis variation in yield strength dominates the along-axis variation in stress accumulation. Conversely, Mode E faults are predicted to develop in environments where enhanced stress accumulation toward the segment ends overcomes the variation in yield strength. The plastic deformation zone associate with Mode E faults is predicted to be broader in across-axis extent than that of Mode C faults, potentially indicating that Mode E faults will initiate and remain active over a wider across-axis region.

High resolution mapping of the slow-spreading Mid-Atlantic Ridge has shown both Mode C and Mode E faults to be prevalent features of many segments, with large Mode E faults typically forming on inside-corner crust. Our calculations show that along-axis variations in Young's modulus alone do not appear to be sufficient to generate the stress gradients necessary for Mode E faulting at many slow-spreading segments. Therefore, we propose a model in which temporal changes in magma supply affect both along-axis gradients in the stresses and mechanical properties of the lithosphere and the stress conditions along the transform fault. During periods of enhanced magmatic activity, the ratio of ridge-to-transform stress, $\sigma_{\mathrm{R}}/\sigma_{\mathrm{T}}$, is predicted to decrease, generating larger stresses at inside corners and concentrating Mode E faulting in these locations. The lack of strong along-axis gradients in stress and lithospheric strength at fast-spreading ridges is predicted to generate a more uniform pattern of faulting as observed at the East Pacific Rise. The results of this study illustrate that the interplay between the along-axis variations in stress state and the mechanical properties of the lithosphere play an important role in controlling the style of fault development at a mid-ocean ridge spreading segment.

Appendix: Thin-plate stress solution for linearly varying Young's modulus

Stress and Strain within the Plate

In this section we present an analytical solution for stress and strain in a thin elastic plate with a linear gradient in Young's modulus from the center of a segment to its distal ends (see

Figure 6). For a plate in plane stress, the stress, σ, and strain, ε, components can be written as

$$\begin{aligned} \sigma_{\mathrm{x}} &= \sigma_{\mathrm{x}}(\mathrm{x},\mathrm{y}) \\ \sigma_{\mathrm{y}} &= \sigma_{\mathrm{y}}(\mathrm{x},\mathrm{y}) \\ \tau_{\mathrm{xy}} &= \tau_{\mathrm{xy}}(\mathrm{x},\mathrm{y}) \\ \tau_{\mathrm{xz}} = \tau_{\mathrm{yz}} &= \sigma_{\mathrm{z}} = 0 \end{aligned} \tag{A1}$$

We define a coordinate system with the x-axis oriented across the ridge axis and the y-axis aligned along the ridge axis. The dimensions of the model space are $2\mathrm{x}_\circ$ and $2\mathrm{y}_\circ$. Small displacements, $\Delta\mathrm{u}_\mathrm{x}$ and $-\Delta\mathrm{u}_\mathrm{x}$, are imposed at the right- and left-hand sides of the model space, respectively. The top and bottom boundaries are assumed to be free slip

$$\tau_{\mathrm{xy}} = 0\Big|_{\text{at } \mathrm{y}=\pm\mathrm{y}_\circ} \tag{A2}$$

with no y-displacement

$$\mathrm{u}_{\mathrm{y}} = 0\Big|_{\text{at } \mathrm{y}=\pm\mathrm{y}_\circ} \tag{A3}$$

The stress and strain relationships for a thin-plate in plane stress [*Jaeger and Cook*, 1979] can be written as

$$\varepsilon_{\mathrm{x}} = \frac{1}{\mathrm{E(y)}}\left[\sigma_{\mathrm{x}} - \nu\sigma_{\mathrm{y}}\right] \tag{A4}$$

and

$$\varepsilon_{\mathrm{y}} = \frac{1}{\mathrm{E(y)}}\left[\sigma_{\mathrm{y}} - \nu\sigma_{\mathrm{x}}\right] \tag{A5}$$

where ν is Poisson's ratio and E(y) is Young's modulus, which varies linearly along the y-axis

$$\mathrm{E(y)} = \mathrm{E}^\circ + (\mathrm{dE/dy})\,|\mathrm{y}| \tag{A6}$$

where dE/dy is a constant. Note that because there is no across-axis gradient in Young's modulus, the far-field strain, $\varepsilon_{\mathrm{x}}^{\mathrm{f.f}} = \Delta\mathrm{u}_\mathrm{x}/\mathrm{x}_\circ$, is constant at all points in the model space for a

given time step. Since no y-displacement is allowed along the top and bottom boundaries, at any x value the integrated strain in the y-direction must sum to zero

$$\int_{-y_\circ}^{y_\circ} \varepsilon_y dy = 0 \tag{A7}$$

Solving Equations A4, A5, and A7 under the condition that σ_y remains constant, we arrive at the following expressions for stress and strain within the plate for any given far-field strain, $\varepsilon_x^{f.f.}$

$$\sigma_y = \frac{\nu \varepsilon_x^{f.f.} (dE/dy)\, y_\circ}{(1-\nu^2) \ln\left[\frac{(dE/dy)\, y_\circ - E^\circ}{E^\circ}\right]} \tag{A8}$$

$$\sigma_y (x) = \left[(dE/dy)\,|y| + E^\circ\right] \varepsilon_x^{f.f.} - \nu \sigma_y \tag{A9}$$

$$\varepsilon_y (y) = \left[\frac{1-\nu^2}{(dE/dy)\,|y| + E^\circ}\right] \sigma_y - \nu \varepsilon_x^{f.f.} \tag{A10}$$

We note that σ_x and ε_y are solely functions of y. Due to the stress-free boundary conditions and uni-axial extension applied to the model, the shear-stresses are negligible. Numerical models show that the addition of an across-axis gradient in Young's modulus, dE/dx, with

$$\frac{\int_{-x_\circ}^{x_\circ} E(x,0)\, dx}{2x_\circ} = E^\circ \tag{A11}$$

will generate effective stresses at the ridge-axis which differ by less than 0.25% from the case of dE/dx = 0, for values of dE/dx similar to that observed at segment OH-1 (Figure 5a).

Calculation of Initial Failure

Perfect plasticity is characterized by a mechanical yield stress, σ_{yield}, beyond which permanent strain appears. In this study, we assume failure of a thin-plate will follow the Von-Mises yield criterion, defined as

$$\sigma_{eff} \geq \sigma_{yield} \tag{A12}$$

where

$$\sigma_{\text{eff}} = \sqrt{\frac{1}{2}\left[\left(\sigma_{\text{x}} - \sigma_{\text{y}}\right)^2 + \sigma_{\text{x}}^2 + \sigma_{\text{y}}^2 + 6\tau_{\text{xy}}^2\right]} \tag{A13}$$

At any point in the plate the yield strength is assumed to be a linear function of x and y, with

$$\begin{aligned}\sigma_{\text{yield}}\left(\text{x},\text{y}\right) = \sigma_{\text{yield}}^{\circ} &+ \left(\text{d}\sigma_{\text{yield}}/\text{dx}\right)\left|\text{x}\right| \\ &+ \left(\text{d}\sigma_{\text{yield}}/\text{dy}\right)\left|\text{y}\right|\end{aligned} \tag{A14}$$

Because the across-axis gradient in yield strength, $\text{d}\sigma_{\text{yield}}/\text{dx}$, is positive and the effective stress, σ_{eff}, varies only in the y-direction (see Equations A8 & A9), initial yielding must occur at the ridge axis where x = 0. Therefore, we can solve for the value of the far-field strain when yielding occurs, $\varepsilon_{@\,\text{yield}}^{\text{f.f.}}$, which is a function of y only:

$$\varepsilon_{@\,\text{yield}}^{\text{f.f.}}\left(\text{y}\right) = \frac{\sigma_{\text{yield}}\left(\text{y}\right)}{\sqrt{\text{A} + \text{B} + \text{C}}} \tag{A15}$$

where

$$\text{A} = \left[\left(\text{dE}/\text{dy}\right)\left|\text{y}\right| + \text{E}^{\circ}\right]^2$$

$$\text{B} = \frac{\left[\left(\text{dE}/\text{dy}\right)\left|\text{y}\right| + \text{E}^{\circ}\right]\left(2\nu^2 - \nu\right)\left(\text{dE}/\text{dy}\right)\text{y}_{\circ}}{\left(1-\nu^2\right)\ln\left[\dfrac{\left(\text{dE}/\text{dy}\right)\left|\text{y}\right| + \text{E}^{\circ}}{\text{E}^{\circ}}\right]}$$

$$\text{C} = \frac{\left(\nu^4 - \nu^3 + \nu^2\right)\left(\text{dE}/\text{dy}\right)^2\text{y}_{\circ}^2}{\left(1-\nu^2\right)^2\ln^2\left[\dfrac{\left(\text{dE}/\text{dy}\right)\left|\text{y}\right| + \text{E}^{\circ}}{\text{E}^{\circ}}\right]}$$

This relationship is used to determine whether initial failure occurs at the segment center or segment ends, and thus whether Mode C or Mode E faults are preferred.

Acknowledgments. We are grateful to Debbie Smith for providing us with the bathymetry and TOBI data for the MAR segment at 25°10'N and for her insights in understanding mid-ocean ridge processes. Pablo Canales and Cecily Wolfe were extremely helpful in providing us with the seismic data used in this paper. This paper benefited by constructive reviews from Patience Cowie and an anonymous reviewer. We would also like to thank Greg Hirth, Brian Tucholke, Pablo Canales, Wen-lu Zhu, and Laurent Montési for helpful discussion during various stages of this research. Several figures in this paper were produced using the public domain GMT software package [*Wessel and Smith,* 1995]. This research was supported by National Science Foundation Grant OCE-9811924 (J. Lin), NASA Grant SENH99-0318-0160 (M.T. Zuber), and a National Defense Science and Engineering Graduate Fellowship (M.D. Behn). Contribution 10540 of Woods Hole Oceanographic Institution.

References

Ackermann, R., and R. Schlische, Uh-Oh! N<1: Dynamic length-displacement scaling, *Eos Trans. AGU*, *80*, S328, 1999.

Alexander, R., and K. Macdonald, Sea Beam, Sea MARC II, and ALVIN-based investigations of faulting on the East Pacific Rise 9°20'–9°50'N, *Mar. Geophys. Res.*, *18*, 557–587, 1996.

Allerton, S., B. Murton, R. Searle, and M. Jones, Extensional faulting and segmentation of the Mid-Atlantic Ridge north of the Kane fracture zone (24°00'N to 24°40'N), *Mar. Geophys. Res.*, *17*, 37–61, 1995.

Barnett, J., J. Mortimer, J. Rippon, J. Walsh, and J. Watterson, Displacement geometry in the volume containing a single normal fault, *Am. Assoc. Petro. Geol. Bull.*, *71*, 925–937, 1987.

Bass, J., Elasticity of minerals, glasses, and melts, in *Mineral Physics and Crystallography: A Handbook of Physical Constants*, edited by T. Ahrens, pp. 45–63, Am. Geophys. Union, Washington, D.C., 1995.

Bathe, K.-J., *Finite Element Procedures*, Prentice Hall, New Jersey, 1996.

Bicknell, J., J.-C. Sempéré, K. Macdonald, and P. Fox, Tectonics of a fast spreading center: A deep-tow and Sea Beam survey on the East Pacific Rise at 19°30'S, *Mar. Geophys. Res.*, *9*, 25–45, 1987.

Bohnenstiehl, D., and M. Kleinrock, Faulting and fault scaling on the median valley floor of the trans-Atlantic geotraverse (TAG) segment, ~26°N on the Mid-Atlantic Ridge, *J. Geophys. Res.*, *104*, 29,351–29,364, 1999.

Brace, W., and D. Kohlstedt, Limits on lithospheric stress imposed by laboratory experiments, *J. Geophys. Res.*, *85*, 6248–6252, 1980.

Bratt, S., and S. Solomon, Compressional and shear wave structure of the East Pacific Rise at 11°20'N: Constraints from three-component ocean bottom seismometer data, *J. Geophys. Res.*, *89*, 6095–6110, 1984.

Briais, A., H. Sloan, L. Parson, and B. Murton, Accretionary processes in the axial valley of the Mid-Atlantic Ridge 27°N–30°N from TOBI side-scan sonar images, *Mar. Geophys. Res.*, *21*, 87–119, 2000.

Buck, W., and A. Poliakov, Abyssal hills formed by stretching oceanic lithosphere, *Nature*, *392*, 272–275, 1998.

Byerlee, J., Friction of rocks, *Pure Appl. Geophys.*, *116*, 615–626, 1978.

Campbell, D., Investigation of the stress-concentration mechanism for intraplate earthquakes, *Geophys. Res. Lett.*, *5*, 477–479, 1978.

Canales, J., J. Collins, J. Escartín, and R. Detrick, Seismic structure across the rift valley of the Mid-Atlantic Ridge at 23°20'N (MARK Area): Implications for crustal accretion processes at slow-spreading ridges, *J. Geophys. Res.*, *105*, 28,411–28,425, 2000a.

Canales, J., R. Detrick, J. Lin, J. Collins, and D. Toomey, Crustal and upper mantle seismic structure beneath the rift mountains and across a nontransform offset at the Mid-Atlantic Ridge (35°N), *J. Geophys. Res.*, *105*, 2699–2719, 2000b.

Canales, J., R. Detrick, D. Toomey, and W. Wilcock, Segment-scale variations in crustal structure of 150- to 300-k.y.-old fast spreading oceanic crust (East Pacific Rise, 8°15'N–10°15'N) from wide-angle seismic refraction profiles, *submitted to Geophys. J. Int.*, 2001.

Cannat, M., et al., Thin crust, ultramafic exposures, and rugged faulting patterns at the Mid-Atlantic Ridge (22°–24°N), *Geology*, *23*, 49–52, 1995.

Carbotte, S., and K. Macdonald, Causes of variation in fault-facing direction on the ocean floor, *Geology*, *18*, 749–752, 1990.

Carbotte, S., and K. Macdonald, Comparison of seafloor tectonic fabric at intermediate, fast, and super fast spreading ridges: Influence of spreading rate, plate motions, and ridge segmentation on fault patterns, *J. Geophys. Res.*, *99*, 13,609–13,631, 1994.

Chen, Y., and W. Morgan, A nonlinear rheology model for mid-ocean ridge axis topography, *J. Geophys. Res.*, *95*, 17,583–17,604, 1990.

Cheng, C., and D. Johnston, Dynamic and static moduli, *Geophys. Res. Lett.*, *8*, 39–42, 1981.

Chopra, P., and M. Paterson, The role of water in the deformation of dunite, *J. Geophys. Res.*, *89*, 7861–7876, 1984.

Christensen, N., and J. Smewing, Geology and seismic structure of the northern section of the Oman ophiolite, *J. Geophys. Res.*, *86*, 2545–2555, 1981.

Collier, J., and S. Singh, Poisson's ratio structure of young oceanic crust, *J. Geophys. Res.*, *103*, 20,981–20,996, 1998.

Cowie, P., Normal fault growth in three-dimensions in continental and oceanic crust, in *Faulting and*

Magmatism at Mid-Ocean Ridges Geophys. Mono. Ser., edited by W. Buck, P. Delaney, J. Karson, and Y. Lagabrielle, vol. 106, pp. 325–348, Am. Geophys. Union, Washington, D.C., 1998.

Cowie, P., C. Scholz, M. Edwards, and A. Malinverno, Fault strain and seismic coupling on mid-ocean ridges, *J. Geophys. Res.*, *98*, 17,911–17,920, 1993.

Crider, J., and D. Pollard, Fault linkage: Three-dimensional mechanical interaction between echelon normal faults, *J. Geophys. Res.*, *103*, 24,373–24,391, 1998.

Detrick, R., H. Needham, and V. Renard, Gravity anomalies and crustal thickness variations along the Mid-Atlantic Ridge between 33°N and 40°N, *J. Geophys. Res.*, *100*, 3767–3787, 1995.

Edwards, M., D. Fornari, A. Malinverno, and W. Ryan, The regional tectonic fabric of the East Pacific Rise from 12°50'N to 15°10'N, *J. Geophys. Res.*, *96*, 7995–8017, 1991.

Eissa, E., and A. Kazi, Relation between static and dynamic Young's modulus, *Int. J. Rock Mech. Min. Sci. Geomech. Abstr.*, *25*, 479–482, 1988.

Escartín, J., G. Hirth, and B. Evans, Effects of serpentinization on the lithospheric strength and the style of normal faulting at slow-spreading ridges, *Earth Planet. Sci. Lett.*, *151*, 181–189, 1997.

Escartín, J., P. Cowie, R. Searle, S. Allerton, N. Mitchell, C. Macleod, and A. Slootweg, Quantifying tectonic strain and magmatic accretion at a slow spreading ridge segment, Mid-Atlantic Ridge, 29°N, *J. Geophys. Res.*, *104*, 10,421–10,437, 1999.

Forslund, T., and A. Gudmundsson, Crustal spreading due to dikes and faults in southwest Iceland, *J. Struct. Geol.*, *13*, 443–457, 1991.

Goetze, C., and B. Evans, Stress and temperature in the bending lithosphere as constrained by experimental rock mechanics, *Geophys. J.R. astr. Soc.*, *59*, 463–478, 1979.

Goff, J., Y. Ma, A. Shah, J. Cochran, and J.-C. Sempéré, Stochastic analysis of seafloor morphology on the flank of the Southeast Indian Ridge: The influence of ridge morphology on the formation of abyssal hills, *J. Geophys. Res.*, *102*, 15,521–15,534, 1997.

Gràcia, E., D. Bideau, R. Hekinian, and Y. Lagabrielle, Detailed geological mapping of two contrasting second-order segments of the Mid-Atlantic Ridge between Oceanographer and Hayes fracture zones (33°30'N–35°N), *J. Geophys. Res.*, *104*, 22,903–22,921, 1999.

Grindlay, N., and P. Fox, Lithospheric stresses associated with nontransform offsets of the Mid-Atlantic Ridge: Implications from a finite element analysis, *Tectonics*, *12*, 982–1003, 1993.

Gudmundsson, A., Effect of tensile stress concentration around magma chambers of intrusion and extrusion frequencies, *J. Volc. Geotherm. Res.*, *35*, 179–194, 1988.

Hirth, G., J. Escartín, and J. Lin, The rheology of the lower oceanic crust: Implications for lithospheric deformation at mid-ocean ridges, in *Faulting and Magmatism at Mid-Ocean Ridges, Geophys. Mono. Ser.*, edited by W. Buck, P. Delaney, J. Karson, and Y. Lagabrielle, vol. 106, pp. 291–303, AGU, Washington, D.C., 1998.

Hooft, E., R. Detrick, D. Toomey, J. Collins, and J. Lin, Crustal thickness and structure along three contrasting spreading segments of the Mid-Atlantic Ridge, $33.5°$–$35°$N, *J. Geophys. Res.*, *105*, 8205–8226, 2000.

Horen, H., M. Zamora, and G. Dubuisson, Seismic wave velocities and anisotropy in serpentinized peridotites from Xigaze ophiolite: Abundance of serpentinite in slow spreading ridge, *Geophys. Res. Lett.*, *23*, 9–12, 1996.

Jaeger, J., and N. Cook, *Fundamentals of Rock Mechanics*, Chapman and Hall, London, 1979.

Kanamori, H., and D. Anderson, Theoretical basis of some empirical relations in seismology, *Bull. Seis. Soc. Am.*, *65*, 1073–1095, 1975.

Karson, J., and A. Winters, Along-axis variations in tectonic extension and accommodation zones in the MARK Area, Mid-Atlantic Ridge $23°$N latitude, in *Ophiolites and their Modern Oceanic Analogues*, edited by L. Parson, B. Murton, and P. Browning, pp. 107–116, Geol. Soc. of London, 1992.

Karson, J., et al., Along-axis variations in seafloor spreading in the MARK area, *Nature*, *328*, 681–685, 1987.

Kuo, B., and D. Forsyth, Gravity anomalies of the ridge-transform system in the South Atlantic between $31°$ and $34.5°$S: Upwelling centers and variations in crustal thickness, *Mar. Geophys. Res.*, *10*, 205–232, 1988.

Lin, J., and E. Parmentier, A finite amplitude necking model of rifting in brittle lithosphere, *J. Geophys. Res.*, *95*, 4909–4923, 1990.

Lin, J., G. Purdy, H. Schouten, J.-C. Sempéré, and C. Zervas, Evidence from gravity data for focused magmatic accretion along the Mid-Atlantic Ridge, *Nature*, *344*, 627–632, 1990.

Macdonald, K., Mid-ocean ridges: Fine scale tectonic, volcanic and hydrothermal processes within the plate boundary zone, *Ann. Rev. Earth Planet. Sci.*, *10*, 155–190, 1982.

Mackwell, S., M. Zimmerman, and D. Kohlstedt, High-temperature deformation of dry diabase with application to tectonics on Venus, *J. Geophys. Res.*, *103*, 975–984, 1998.

Malinverno, A., and P. Cowie, Normal faulting and the topographic roughness of mid-ocean ridge flanks, *J. Geophys. Res.*, *98*, 17,921–17,939, 1993.

Miller, D., and N. Christensen, Seismic velocities of the lower crustal and upper mantle rocks from the slow spreading Mid-Atlantic Ridge, south of the Kane transform zone (MARK), in *Proc. Ocean Drill. Program Sci. Results*, vol. 153, pp. 437–454, College Station, TX, 1997.

Pariso, J., J.-C. Sempéré, and C. Rommevaux, Temporal and spatial variations in crustal accretion along the Mid-Atlantic Ridge (29°–31°30'N) over the last 10 m.y.: Implications from a three-dimensional gravity study, *J. Geophys. Res.*, *100*, 17,781–17,794, 1995.

Phipps Morgan, J., and D. Forsyth, Three-dimensional flow and temperature perturbations due to a transform offset: Effects on oceanic crust and upper mantle structure, *J. Geophys. Res.*, *93*, 2955–2966, 1988.

Phipps Morgan, J., and E. Parmentier, Lithospheric stress near a ridge-transform intersection, *Geophys. Res. Lett.*, *11*, 113–116, 1984.

Phipps Morgan, J., E. Parmentier, and J. Lin, Mechanisms for the origin of mid-ocean ridge axial topography: Implications for the thermal and mechanical structure of accreting plate boundaries, *J. Geophys. Res.*, *92*, 12,823–12,836, 1987.

Poliakov, A., and W. Buck, Mechanics of strectching elastic-plastic-viscous layers: Applications to slow-spreading mid-ocean ridges, in *Faulting and Magmatism at Mid-Ocean Ridges, Geophys. Mono. Ser.*, edited by W. Buck, P. Delaney, J. Karson, and Y. Lagabrielle, vol. 106, pp. 305–323, AGU, Washington, D.C., 1998.

Pollard, D., and A. Aydin, Propagation and linkage of oceanic ridge segments, *J. Geophys. Res.*, *89*, 10,017–10,028, 1984.

Purdy, G., J.-C. Sempéré, H. Schouten, D. Dubois, and R. Goldsmith, Bathymetry of the Mid-Atlantic Ridge, 24°–31°N: A map series, *Mar. Geophys. Res.*, *12*, 247–252, 1990.

Searle, R., GLORIA survey of the East Pacific Rise near 3.5°S: Tectonic and volcanic characteristics of a fast spreading mid-ocean rise, *Tectonophys.*, *101*, 319–344, 1984.

Searle, R., and A. Laughton, Fine-scale sonar study of tectonics and volcanism on the Reykjanes Ridge, *Oceanol. Acta*, *4 suppl.*, 5–13, 1981.

Searle, R., P. Cowie, N. Mitchell, S. Allerton, C. MacLeod, J. Escartín, S. Russell, P. Slootweg, and T. Tanaka, Fault structure and detailed evolution of a slow spreading ridge segment: the Mid-Atlantic Ridge at 29°N, *Earth Planet. Sci. Lett.*, *154*, 167–183, 1998.

Sempéré, J.-C., J. Lin, H. Brown, H. Schouten, and G. Purdy, Segmentation and morphotectonic variations along a slow-spreading center: The Mid-Atlantic ridge (24°00'N–30°40'N), *Mar. Geophys. Res.*, *15*, 153–200, 1993.

Severinghaus, J., and K. Macdonald, High inside corners at ridge-transform intersections, *Mar. Geophys. Res.*, *9*, 353–367, 1988.

Shaw, P., Ridge segmentation, faulting and crustal thickness in the Atlantic Ocean, *Nature*, *358*, 490–493, 1992.

Shaw, P., and J. Lin, Causes and consequences of variations in faulting style at the Mid-Atlantic Ridge, *J. Geophys. Res.*, *98*, 21,839–21,851, 1993.

Shaw, W., and J. Lin, Models of ocean ridge lithospheric deformation: Dependence on crustal thickness, spreading rate, and segmentation, *J. Geophys. Res.*, *101*, 17,977–17,993, 1996.

Smith, D., et al., Mid-Atlantic Ridge volcanism from deep-towed side-scan sonar images, 25°–29°N, *J. Volc. Geotherm. Res.*, *67*, 233–262, 1995.

Spyropoulos, C., W. Griffith, C. Scholz, and B. Shaw, Experimental evidence for different strain regimes of crack populations in a clay model, *Geo. Res. Lett.*, *26*, 1081–1084, 1999.

Tapponnier, P., and J. Francheteau, Necking of the lithosphere and the mechanics of slowly accreting plate boundaries, *J. Geophys. Res.*, *83*, 3955–3970, 1978.

Tolstoy, M., A. Harding, and J. Orcutt, Crustal thickness on the Mid-Atlantic Ridge: Bull's-eye gravity anomalies and focused accretion, *Science*, *262*, 726–729, 1993.

Tucholke, B., and J. Lin, A geological model for the structure of ridge segments in slow spreading ocean crust, *J. Geophys. Res.*, *99*, 11,937–11,958, 1994.

Tucholke, B., J. Lin, M. Kleinrock, M. Tivey, T. Reed, J. Goff, and G. Jaroslow, Segmentation and crustal structure of the western Mid-Atlantic Ridge flank, 25°25'–27°10'N and 0–29 m.y., *J. Geophys. Res.*, *102*, 10,203–10,223, 1997.

Tuckwell, G., J. Bull, and D. Sanderson, Numerical models of faulting at oblique spreading centers, *J. Geophys. Res.*, *103*, 15,473–15,482, 1998.

Walsh, J., and J. Watterson, Distributions of cumulative displacement and seismic slip on a single normal fault surface, *J. Struct. Geol.*, *9*, 1039–1046, 1987.

Watts, A., J. Bodine, and M. Steckler, Observations of flexure and the state of stress in the oceanic lithosphere, *J. Geophys. Res.*, *85*, 6369–6376, 1980.

Weiland, C., K. Macdonald, and N. Grindlay, Ridge segmentation and the magnetic structure of the Southern Mid-Atlantic Ridge 26°S and 31°–35°S: Implications for magmatic processes at slow spreading centers, *J. Geophys. Res.*, *101*, 8055–8073, 1996.

Wolfe, C., G. Purdy, D. Toomey, and S. Solomon, Microearthquake characteristics and crustal velocity structure at 29°N on the Mid-Atlantic Ridge: The architecture of a slow spreading segment, *J. Geophys. Res.*, *100*, 24,449–24,472, 1995.

M. D. Behn, MIT/WHOI Joint Program, Woods Hole Oceanographic Institution, Woods Hole, MA 02543 (mbehn@mit.edu)

J. Lin, Department of Geology and Geophysics, Woods Hole Oceanographic Institution, Woods Hole, MA 02543 (jlin@whoi.edu)

M. T. Zuber, Department of Earth, Atmospheric and Planetary Sciences, Massachusetts Institute of Technology, Cambridge, MA 02139 (zuber@mit.edu)

Received _____

Revised for Journal of Geophysical Research, October, 2001

This manuscript was prepared with AGU's LaTeX macros v4, with the extension package 'AGU++' by P. W. Daly, version 1.6a from 1999/05/21.

Figure Captions

Figure 1. Geologic maps from *Gràcia et al.* [1999] of (a) MAR segment OH-1 and (b) segment OH-3 based on a combination of bathymetry, acoustic backscattering, submersible observations, and rock samples. Major fault scarps are shown in black. At both segments, faults appear to develop not only near segment center (Mode C faults), but also toward segment ends (Mode E faults). Note the asymmetry in faulting toward the segment ends, with most major faults forming on the inside-corner crust near the Oceanographer fracture zone (in a) and non-transform offsets NTO2 and NTO3 (in b). Figure from *Gràcia et al.* [1999]

Figure 2. (a) Multi-beam bathymetry from *Purdy et al.* [1990] and *Smith et al.* [1995] for the MAR segment at 25°10'N. Note the hour-glass shape morphology of the axial valley, which is characteristic of many magmatically robust slow-spreading segments. (b) Geologic map of the 25°10'N segment based on the multi-beam bathymetry data in (a) and TOBI side-scan sonar data from *Smith et al.* [1995]. Dashed line delineates the area within which the TOBI data are available. Throw of faults was measured along major fault scarps, and location of maximum throw is marked with a star. Note that major faults develop not only at the segment center (Mode C faults), but also near the segment ends (Mode E faults), particularly on inside-corner crust.

Figure 3. (a) Seismic P-wave velocity model of *Canales et al.* [2000b] along the western rift mountains of MAR segment OH-1 (see Figure 4 for location). Segment is bounded to the south by a non-transform offset and to the north by the Oceanographer fracture zone. (b) Calculated dynamic Young's modulus with depth along the OH-1 segment, based on the P-wave velocity and density models of *Canales et al.* [2000b] and assuming a Poisson's ratio of 0.30. See text for description of dynamic Young's modulus calculation. (c) Calculated yield strength depth section along the OH-1 segment. Yield strength is based on Byerlee's rule with a constant coefficient of friction $\mu = 0.85$, above the brittle/ductile transition and the ductile flow law below the brittle/ductile transition. We assume the dry diabase flow law of *Mackwell et al.* [1998] for the crust and *Chopra and Paterson* [1984] dry dunite flow law for the mantle. The thermal structure for the OH-1 segment was calculated using *Phipps Morgan and Forsyth* [1988] passive flow model with a half rate of 1.1 cm/yr and a mantle temperature of 1350°C at a depth of 100 km.

Figure 4. (a) Along-axis variation in the calculated Young's modulus averaged to a depth of 8 km based on the seismic refraction profiles of *Canales et al.* [2000b] (dashed) and *Hooft et al.* [2000] (solid). (b) Location of *Canales et al.* [2000b] and *Hooft et al.* [2000] seismic lines. (c) Along-axis variation in the calculated yield strength averaged to a depth of 15 km along the *Canales et al.* [2000b] and *Hooft et al.* [2000] seismic lines. See Figure 3 for description of parameters used in calculation of yield strength. Gray bars illustrate the location of the non-transform offset (NTO) and Oceanographer fracture zone (OFZ) bounding the OH-1 segment to the south and north, respectively. Small arrow shows segment mid-point. (d,e,f) Calculated Young's modulus, location, and yield strength, respectively, for two profiles through the 3-D tomographic P-wave inversion of *Wolfe et al.* [1995] at 29°N on the MAR. (g,h,i) Calculated Young's modulus, location, and yield strength, respectively, for two seismic refraction profiles *Canales et al.* [2001] on ∼300 k.y.-old crust at 9°N along the EPR. Note that the two MAR segments display significant along-axis gradients in both Young's modulus (0.2–0.3 GPa/km) and yield strength (0.1–1.0 MPa/km), with the lowest values found at the center of the segment. In contrast, the EPR segment shows little variation in either Young's modulus or yield strength along-axis, except within the Siqueiros fracture zone (SFZ) and overlapping spreading center (OSC) at the segment ends.

Figure 5. (a) Two temperature-depth profiles calculated at the center of a 50-km-long northern MAR segment. Dashed line (PM&F88) shows temperatures calculated from the passive flow model of *Phipps Morgan and Forsyth* [1988], assuming a half-rate of 1 cm/yr and a mantle temperature of 1350°C at a depth of 100 km. Solid line (S&L96) illustrates the NMARL thermal model of *Shaw and Lin* [1996] for similar parameters, but incorporates the effects of hydrothermal cooling in the crust and the heat of magma emplacement with variable crustal thickness. (b) Yield strength envelopes computed from thermal models in (a). Yield strength is calculated using Byerlee's rule with a constant coefficient of friction, $\mu = 0.85$, above the brittle/ductile transition and the ductile flow law below the brittle/ductile transition. We assume the dry diabase flow law of *Mackwell et al.* [1998] for the crust and Chopra and Paterson's [1984] dry dunite flow law for the mantle. A strain rate of 10^{-14} s^{-1} was used for all calculations. (c,d) Thermal profiles and corresponding yield strength envelopes calculated at the end of the NMARL segment. Thick gray line illustrates the predicted effect of serpentinization on the brittle regime above the 400°C isotherm when using the coefficient of friction for serpentinite ($\mu = 0.3$) from *Escartín et al.* [1997]. Note that the *Shaw and Lin* [1996] thermal model predicts lower strength at the segment center and greater strength at the segment ends relative to the model of *Phipps Morgan and Forsyth* [1988].

Figure 6. (a) The lithosphere at a mid-ocean ridge segment is modeled as a thin plate in plane stress undergoing uni-axial extension. The model space is 100 km x 100 km, with finer grid spacing toward the ridge axis. The north and south edges of the model are assigned to be free-slip boundaries with no displacement in the y-direction. (b, c) Each element is assigned a Young's Modulus, E, and a yield strength value, σ_{yield}, which are allowed to vary linearly along- and across-axis.

Figure 7. (a, b) Illustration of the relationship between effective stress (thin line) versus yield stress (thick line) at the ridge axis. Failure will occur if the effective stress is greater than the yield stress at any point. Mode C faults (a) develop when the effective stress exceeds the yield stress first at the ridge center. Dashed line illustrates the effective stress for a value of $\varepsilon_x^{f,f\cdot}$ before yielding. Mode E faults (b) develop if the effective stress exceeds the yield strength first at the segment ends. The relative magnitude of the along-axis gradient in Young's modulus (which controls the gradient in effective stress for a given far-field strain) and yield strength dictate whether Mode C or Mode E faults will develop. (c) Calculated plastic strain associated with Mode C faults (propagation from the center of a segment toward its ends) calculated using the ADINA finite-element model. Arrows indicate direction of fault propagation. (d) Calculated plastic strain associated with Mode E faults (propagation from the segment ends toward the segment center). Note that the calculated plastic yield zone associated with Mode E faults is wider than for Mode C faults.

Figure 8. dE/dy versus $d\sigma_{yield}/dy$ phase space showing the mode boundary between Mode E and Mode C faults (thick black line). Shaded contours illustrate the far-field strain necessary for initial yielding. The values of Young's modulus and yield strength at the center of the segment are E° = 75 GPa and σ°_{yield} = 50 MPa, respectively. Gray squares show parameters used in the 5 cases shown in Figure 9. Approximate parameter values of the OH-1 and MAR 29°N segments are shown based on the values of dE/dy and $d\sigma_{yield}/dy$ calculated in Figure 4. Note that when the along-axis gradient in yield strength dominates, Mode C faults are predicted. Conversely, when the along-axis gradient in Young's modulus dominates over the gradient in yield strength, Mode E faults are predicted.

Figure 9. Plastic strain calculated using ADINA with increasing far-field strain for the 5 sets of parameters illustrated in Figure 8. (a,b) Mode E faults. (c) Uniform failure along the entire segment. (d,e) Mode C faults. For a given $\varepsilon_x^{f,f\cdot}$, the plastic deformation zone propagates a greater distance along-axis for the parameters in 9b and 9d than in 9a and 9e.

Figure 10. Mode boundary between Mode E and Mode C faults (thick black line) for four different values of Young's modulus and yield strength at the segment center. (a) E° = 75 GPa, σ°_{yield} = 25 MPa. (b) E° = 75 GPa, σ°_{yield} = 75 MPa. (c) E° = 50 GPa, σ°_{yield} = 50 MPa. (d) E° = 100 GPa, σ°_{yield} = 50 MPa. Shaded contours illustrate the far-field strain necessary for initial yielding. Note the decrease in size of the Mode E phase space as the value of E° becomes larger relative to the value of σ°_{yield}

Figure 11. Contour plot of the additional gradient in σ_{eff}, after accounting for variations due to dE/dy, that is necessary to switch modes of faulting. Approximate parameter values of the OH-1 and MAR 29°N segments are shown based on the values of dE/dy and $d\sigma_{yield}/dy$ calculated in Figure 4. We hypothesize that the additional gradient in σ_{eff} necessary to form the Model E faults observed at the OH-1 and MAR 29°N segments may be generated by a combination of shearing along transform faults and temporal variations in magma supply along the ridge axis.

Figure 12. (a) Contour plot of the calculated change in effective stress, $\Delta\sigma_{RT}$, generated by applying a shear stress, σ_T, along two 30-km-long transform faults. We assume $\sigma_R = \sigma^{\circ}_{yield}$ and set σ_T such that the stress coupling ratio, σ_R/σ_T, is equal to 2. (b,c,d) Along-axis variations in effective stress, with $\varepsilon^{f.f.}_x$ = 6.4e-4, for σ_R/σ_T ratios of 2, 3, and 5, respectively. Solid black lines show the variation in σ_{eff} for the stress-free boundary conditions shown in Figure 6 (i.e., σ_T = 0). Gray lines illustrate σ_{eff} at x = 0, -5, -15, and -25 km, respectively. Note that except for the small region surrounding the point at which the ridge and transform meet, the inside corners are characterized by increased σ_{eff} relative to the outside corners.

Table 1. Model Paramters

	Meaning	Value	Units
ν	Poisson's ratio	0.3	
ρ	density		kg/m^3
μ	coefficient of friction	0.85	
v_p	p-wave velocity		m/s
$x_\circ$	across-axis model space half-width	50	km
$y_\circ$	along-axis model space half-width	50	km
Δu_x	far-field half-dispacement		km
$\varepsilon_x^{f.f.}$	far-field strain in x-direction	$\Delta u_x / x_\circ$	
$\varepsilon_{@\,yield}^{f.f.}$	far-field strain at initial yielding		
E	Young's modulus		GPa
E$^\circ$	Young's modulus at segment center		GPa
dE/dx	across-axis gradient in Young's modulus		GPa/km
dE/dy	along-axis gradient in Young's modulus		GPa/km
σ_{yield}	yield strength		MPa
σ_{yield}°	yield strength at segment center		MPa
dσ_{yield}/dx	across-axis gradient in yield strength	$2 * d\sigma_{yield}$/dy	MPa/km
dσ_{yield}/dy	along-axis gradient in yield strength		MPa/km
σ_{eff}	effective stress		MPa
dσ/dy	additional gradient in σ_{eff} to switch modes of faulting		MPa/km
σ_R	tensile stress resisting plate separation at ridge axis	σ_{yield}°	MPa
σ_T	shear stress resisting plate motion along offset		MPa
$\Delta\sigma_{R\,T}$	change in σ_{eff} due to ridge-transform intersection		MPa

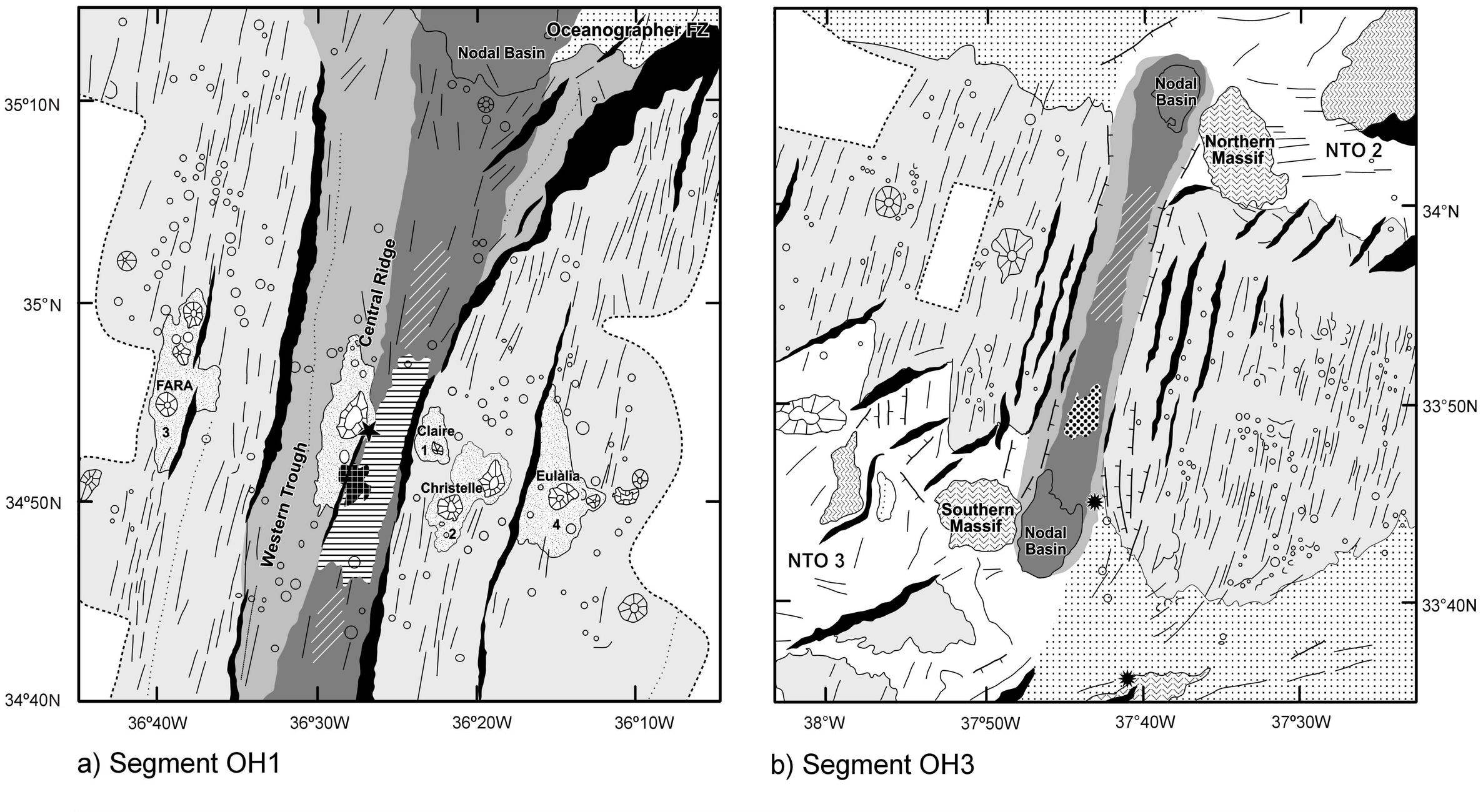
Oceanographer FZ
Nodal Basin
35º10N
35°N
34º50N
34º40N
Central Ridge
Western Trough
FARA
3
Claire
1
Christelle
2
Eulàlia
4
36º40W
36º30W
36º20W
36º10W
a) Segment OH1
Nodal Basin
Northern Massif
NTO 2
34°N
33°50N
Southern Massif
Nodal Basin
NTO 3
33°40N
38°W
37º50W
37°40W
37º30W
b) Segment OH3
axial/inner valley floor
tectonized area
neovolcanics (sheet flow)
neovolcanics (pillow lava)
outer rift valley floor
ridge-flank terrain
volcaniclastic deposits
volcanic alignment
ultramafic massifs
unsampled massifs
sediments
NTO terrain
hydrothermal activity
B. Petrov dredges
1 seamounts
major fault scarp
minor fault scarp
structural lineation
limit of data
low

Figure 1

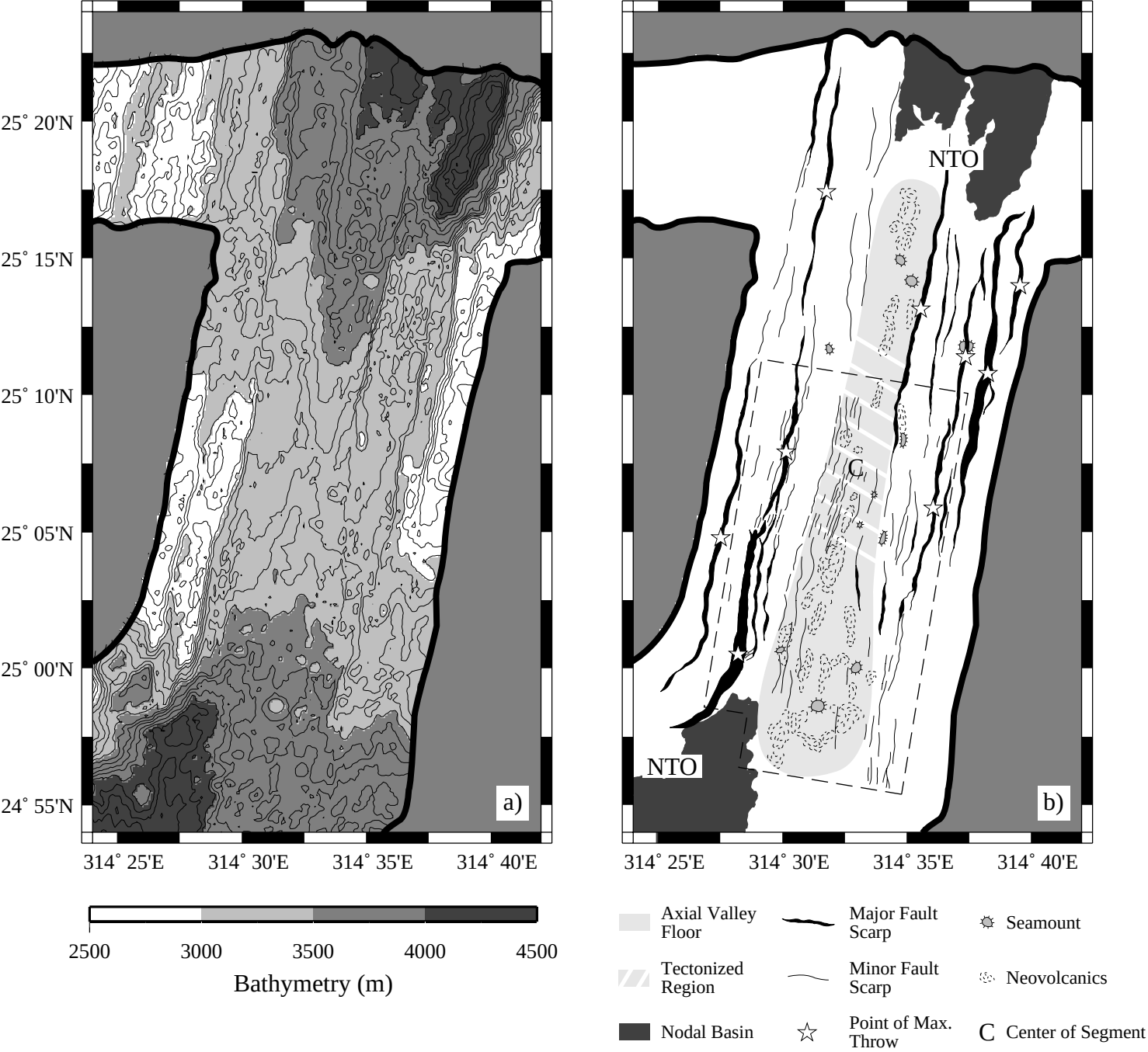
25˚ 20'N
25˚ 15'N
25˚ 10'N
25˚ 05'N
25˚ 00'N
24˚ 55'N
314˚ 25'E
314˚ 30'E
314˚ 35'E
314˚ 40'E
a)
2500
3000
3500
4000
4500
Bathymetry (m)
NTO
C
NTO
b)
Axial Valley Floor
Tectonized Region
Nodal Basin
Major Fault Scarp
Minor Fault Scarp
Point of Max. Throw
Seamount
Neovolcanics
C Center of Segment

Figure 2

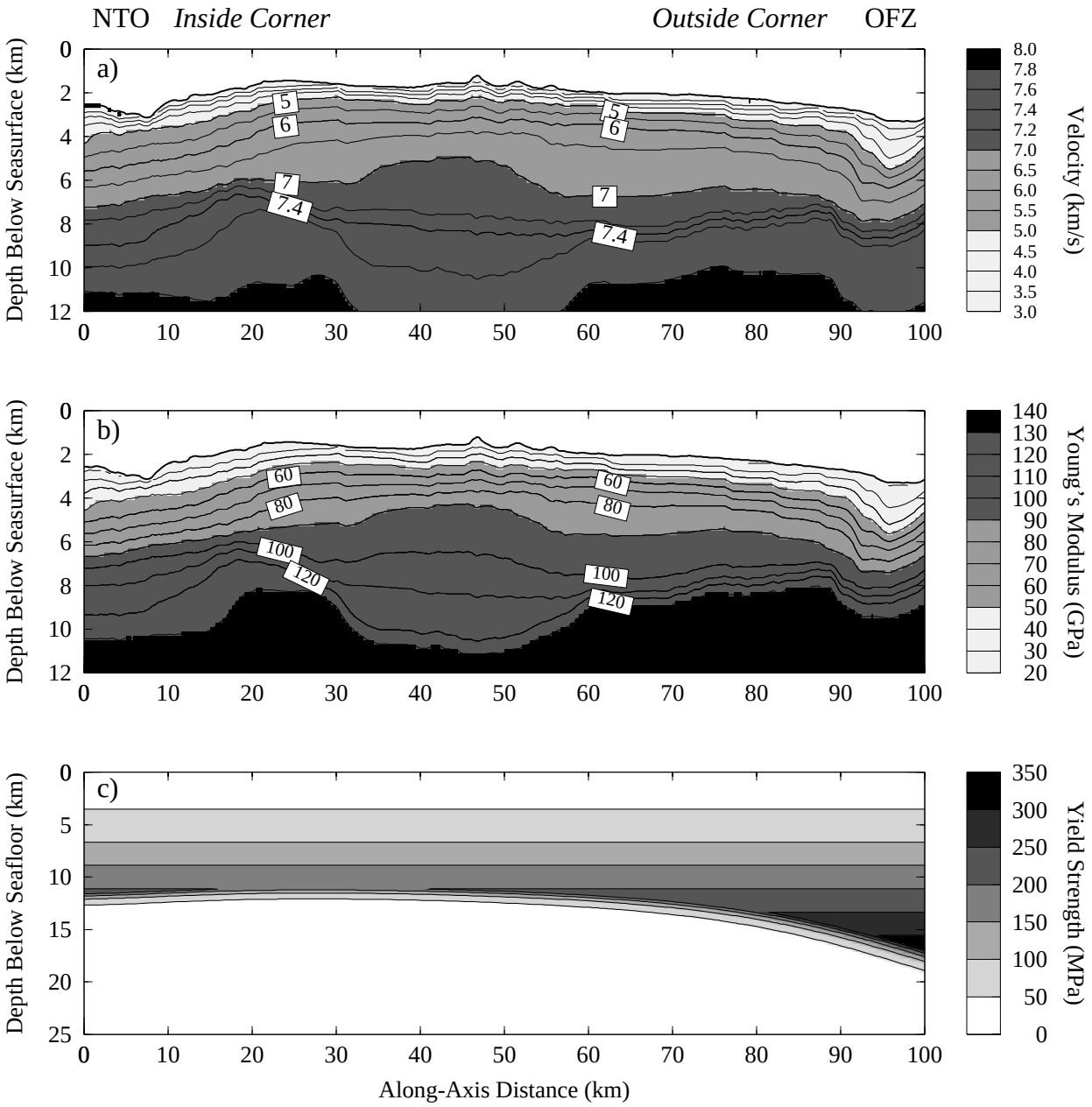
NTO
Inside Corner
Outside Corner
OFZ
a)
b)
c)
Depth Below Seasurface (km)
Depth Below Seafloor (km)
Along-Axis Distance (km)
Velocity (km/s)
Young's Modulus (GPa)
Yield Strength (MPa)
5
6
7
7.4
60
80
100
120

Figure 3

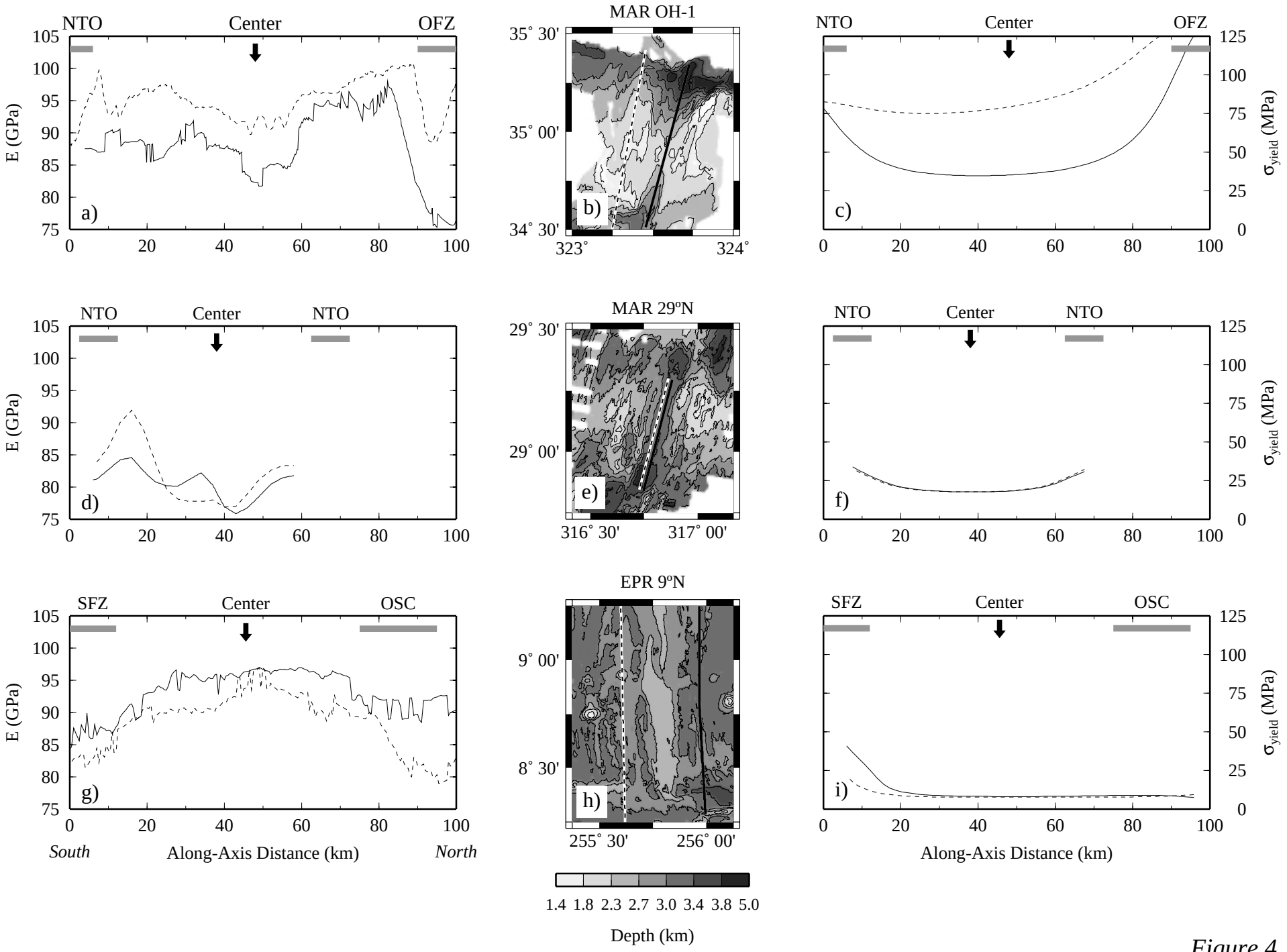
NTO
Center
OFZ
E (GPa)
a)
MAR OH-1
35° 30'
35° 00'
34° 30'
323°
324°
b)
c)
σyield (MPa)
NTO
Center
NTO
d)
MAR 29ºN
29° 30'
29° 00'
316° 30'
317° 00'
e)
f)
SFZ
Center
OSC
g)
EPR 9ºN
9° 00'
8° 30'
255° 30'
256° 00'
h)
i)
South
Along-Axis Distance (km)
North
1.4 1.8 2.3 2.7 3.0 3.4 3.8 5.0
Depth (km)

Figure 4

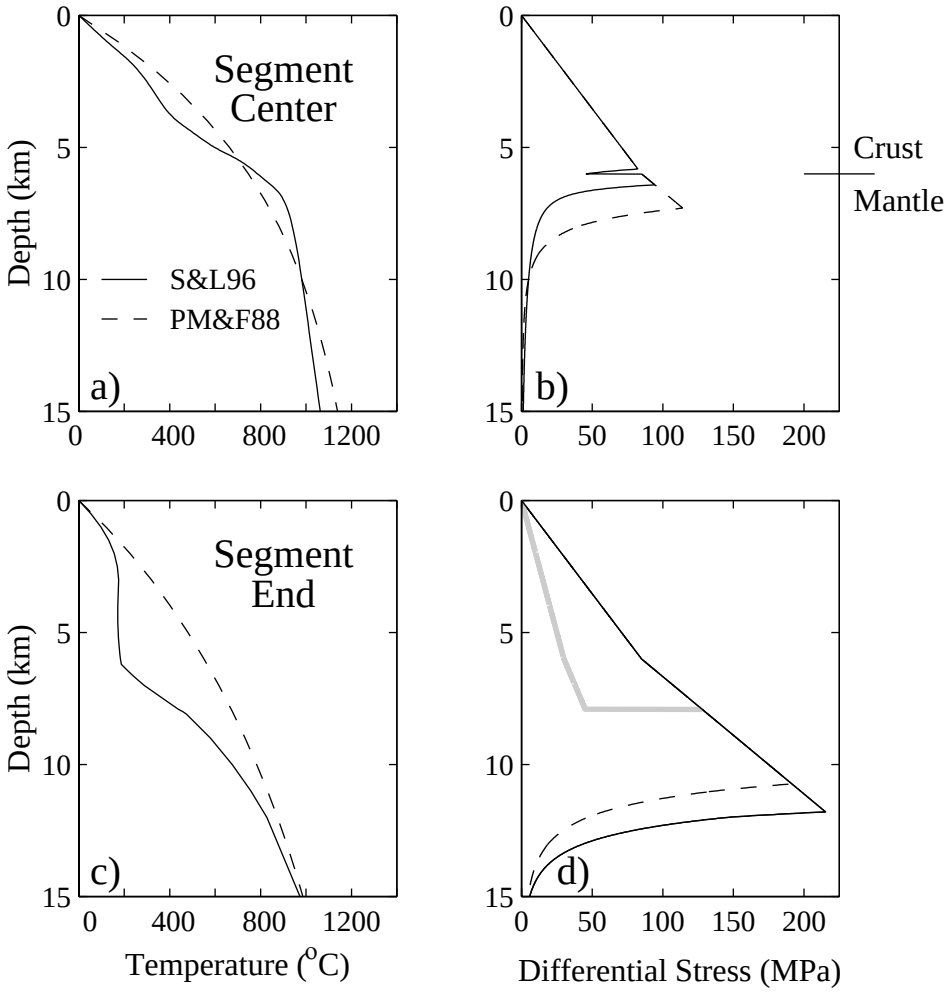
Segment
Center
Depth (km)
S&L96
PM&F88
a)
b)
Crust
Mantle
Segment
End
c)
d)
Temperature (°C)
Differential Stress (MPa)

Figure 5

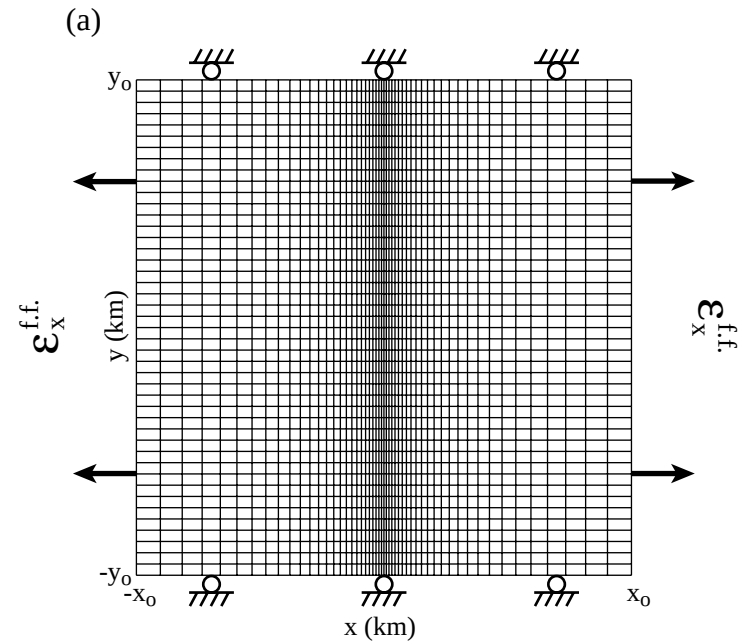

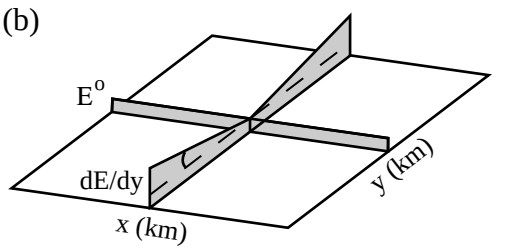

$$E = E^o + (dE/dy)|y|$$

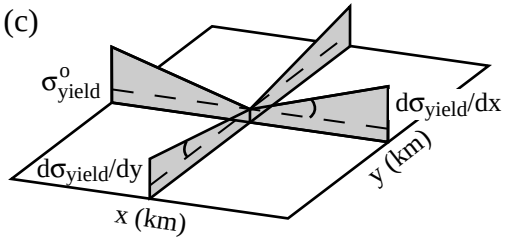

$$\sigma_{yield} = \sigma^o_{yield} + (d\sigma_{yield}/dx)|x| + (d\sigma_{yield}/dy)|y|$$

Figure 6

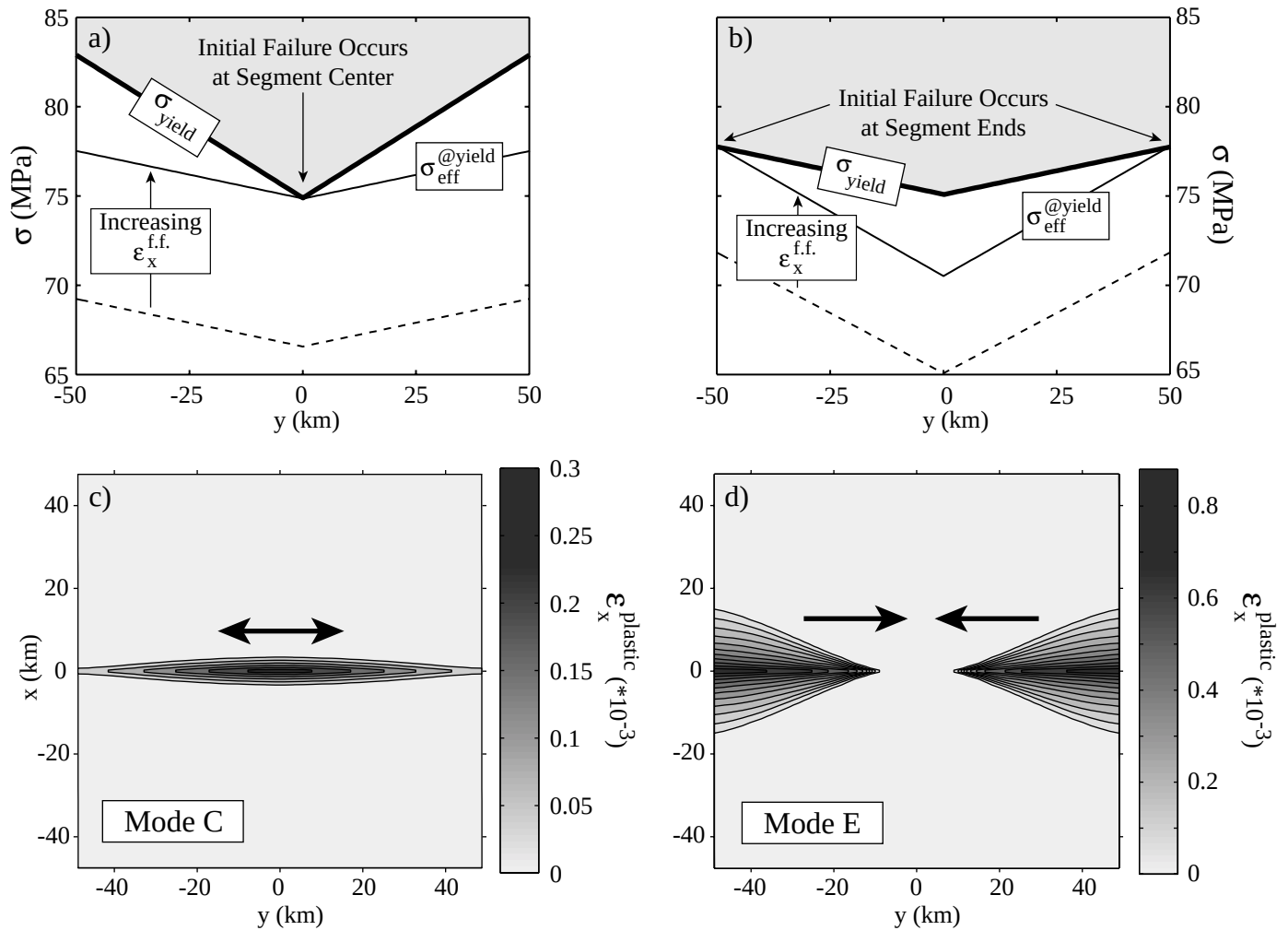
a)
Initial Failure Occurs
at Segment Center
σ yield
σ @yield eff
Increasing
ε f.f. x
σ (MPa)
y (km)
b)
Initial Failure Occurs
at Segment Ends
σ yield
σ @yield eff
Increasing
ε f.f. x
σ (MPa)
y (km)
c)
Mode C
x (km)
y (km)
ε plastic x (*10-3)
d)
Mode E
y (km)
ε plastic x (*10-3)

Figure 7

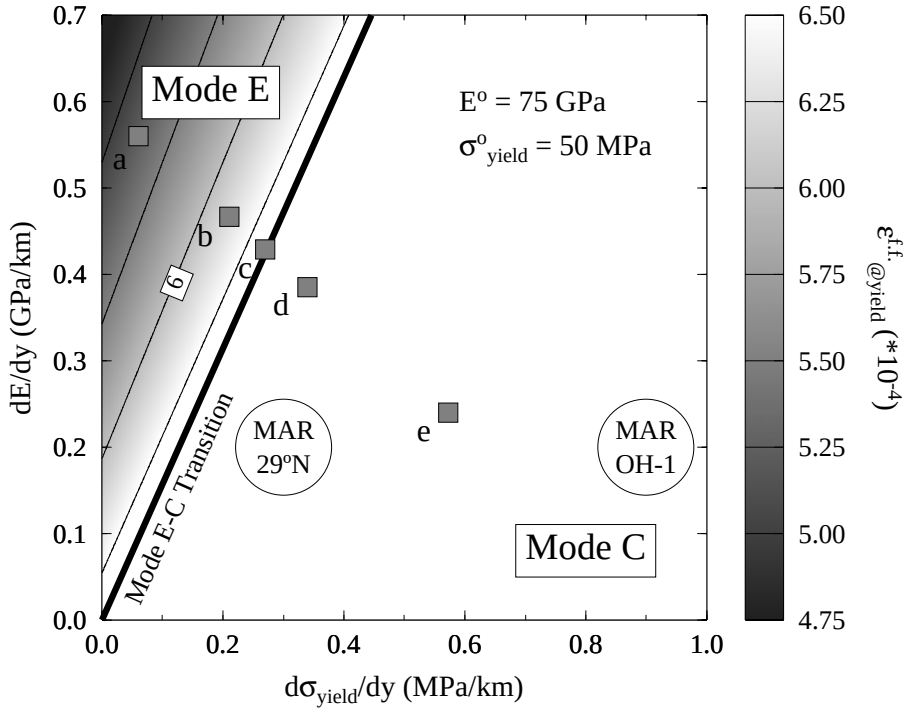
Mode E
Mode C
Mode E-C Transition
E° = 75 GPa
σ°yield = 50 MPa
MAR 29°N
MAR OH-1
a
b
c
d
e
6
dE/dy (GPa/km)
dσyield/dy (MPa/km)
ε f.f.@yield (*10-4)
0.0
0.1
0.2
0.3
0.4
0.5
0.6
0.7
0.0
0.2
0.4
0.6
0.8
1.0
4.75
5.00
5.25
5.50
5.75
6.00
6.25
6.50

Figure 8

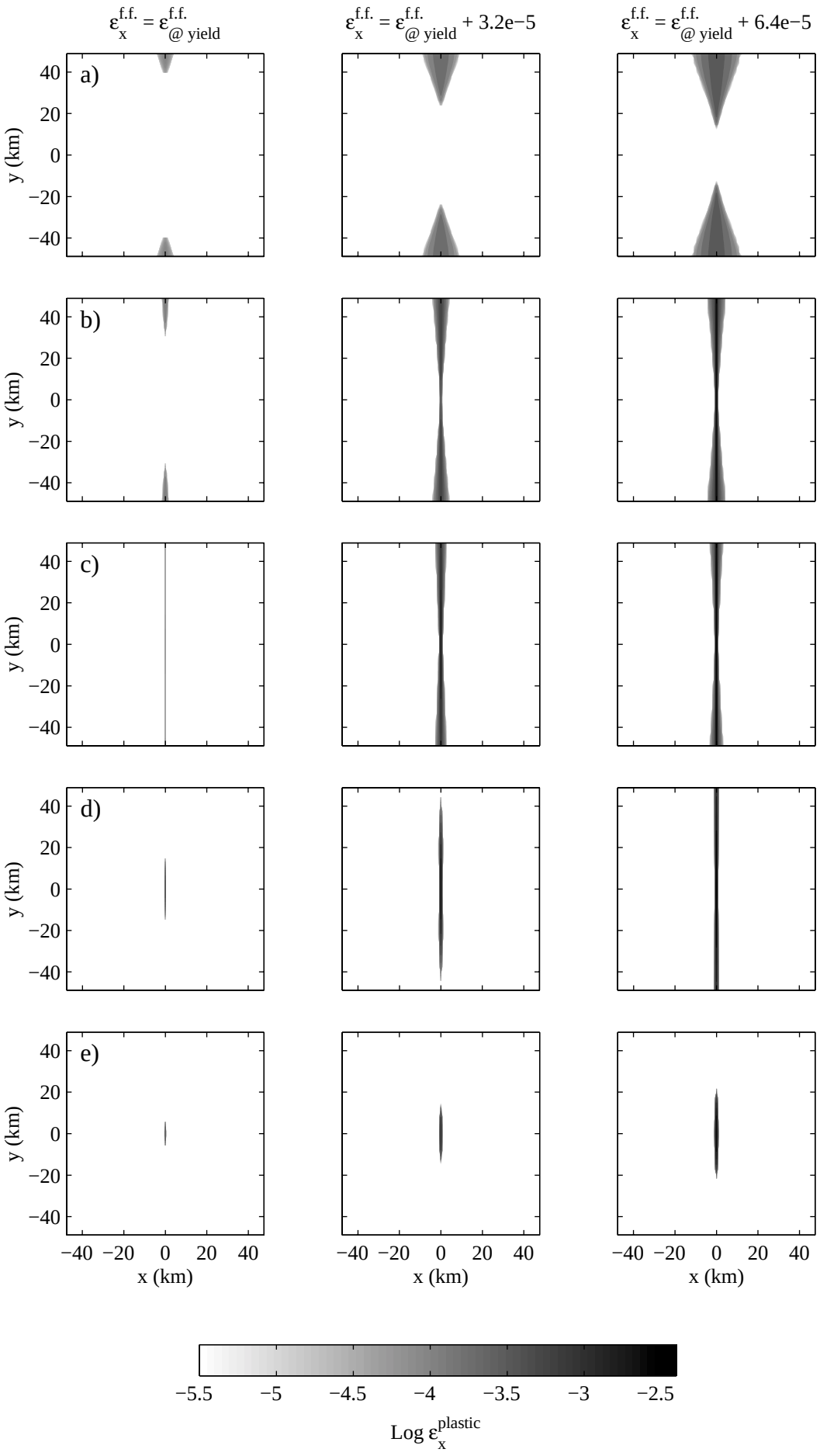
$\varepsilon_x^{f.f.} = \varepsilon_{@\ yield}^{f.f.}$
$\varepsilon_x^{f.f.} = \varepsilon_{@\ yield}^{f.f.} + 3.2e{-}5$
$\varepsilon_x^{f.f.} = \varepsilon_{@\ yield}^{f.f.} + 6.4e{-}5$
a)
b)
c)
d)
e)
y (km)
x (km)
40
20
0
−20
−40
−5.5
−5
−4.5
−4
−3.5
−3
−2.5
Log $\varepsilon_x^{plastic}$

Figure 9

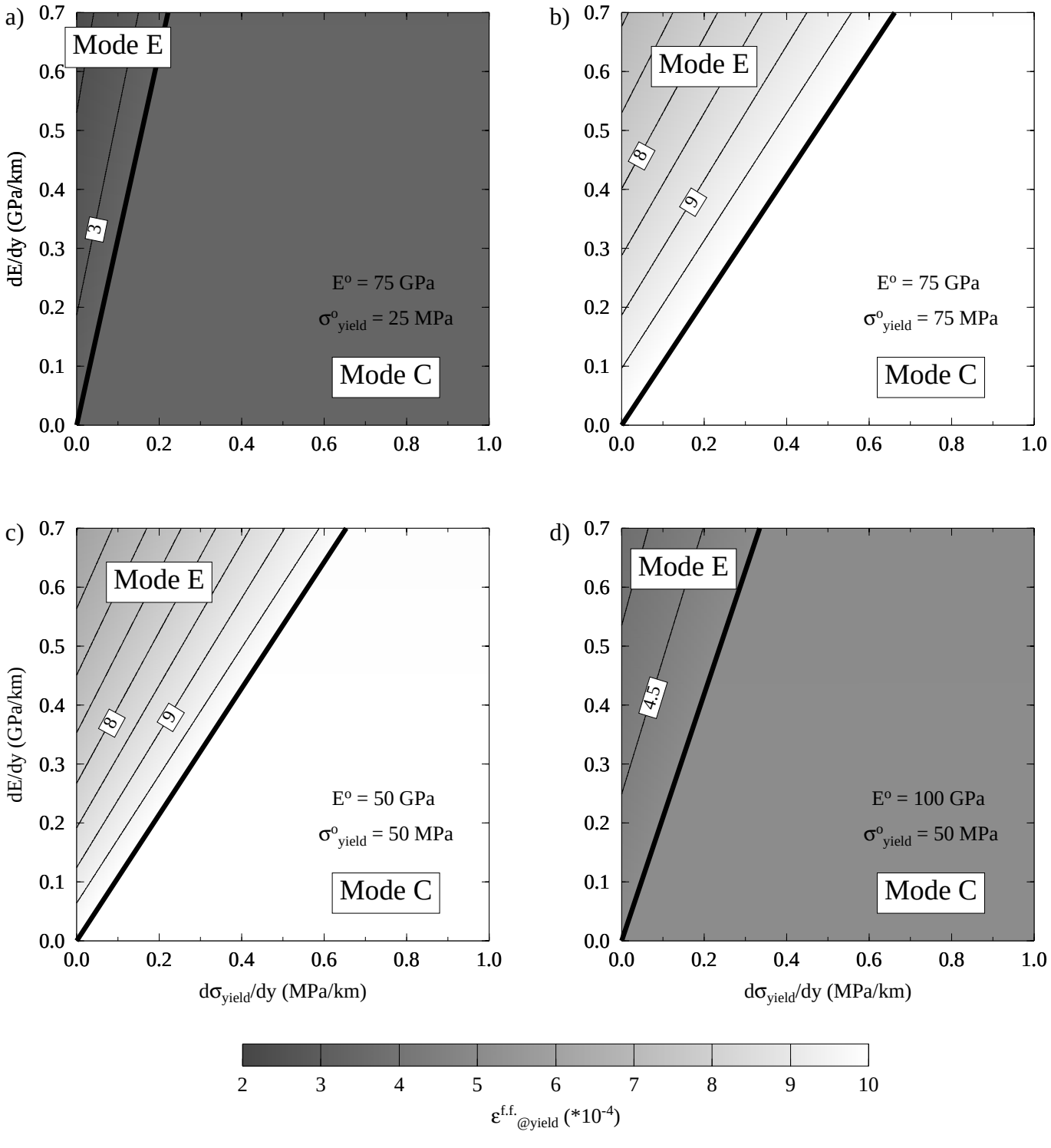
a)
Mode E
Mode C
3
E° = 75 GPa
σ°yield = 25 MPa
b)
Mode E
Mode C
8
9
E° = 75 GPa
σ°yield = 75 MPa
c)
Mode E
Mode C
8
9
E° = 50 GPa
σ°yield = 50 MPa
d)
Mode E
Mode C
4.5
E° = 100 GPa
σ°yield = 50 MPa
dE/dy (GPa/km)
dσyield/dy (MPa/km)
0.0
0.1
0.2
0.3
0.4
0.5
0.6
0.7
0.8
1.0
2
3
4
5
6
7
8
9
10
εf.f.@yield (*10-4)

Figure 10

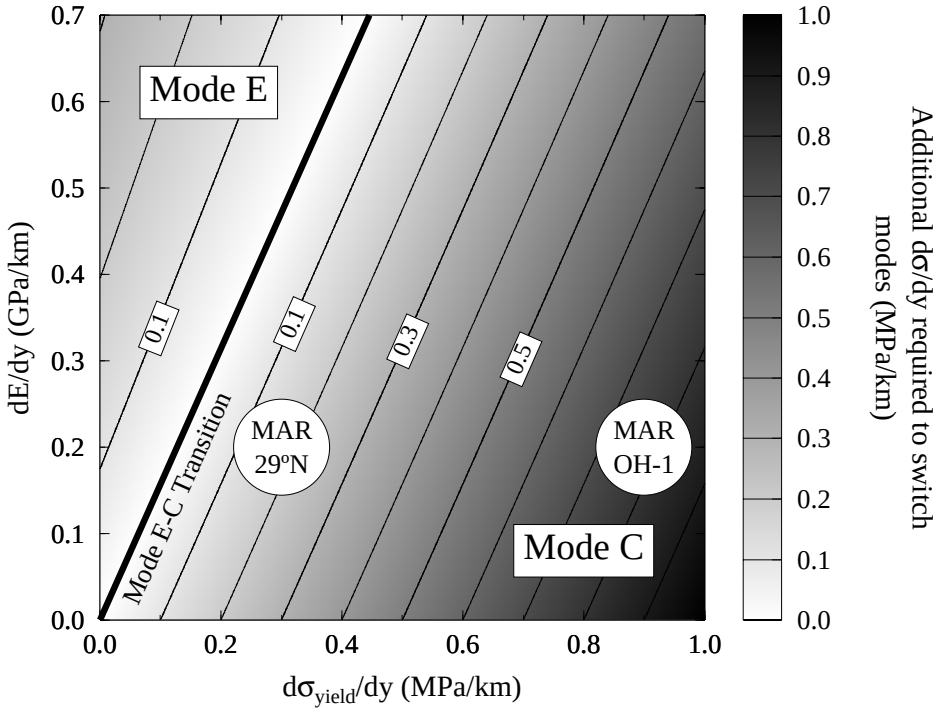
Mode E
Mode C
Mode E-C Transition
0.1
0.1
0.3
0.5
MAR
29ºN
MAR
OH-1
dE/dy (GPa/km)
dσyield/dy (MPa/km)
Additional dσ/dy required to switch modes (MPa/km)
0.0
0.1
0.2
0.3
0.4
0.5
0.6
0.7
0.8
0.9
1.0

Figure 11

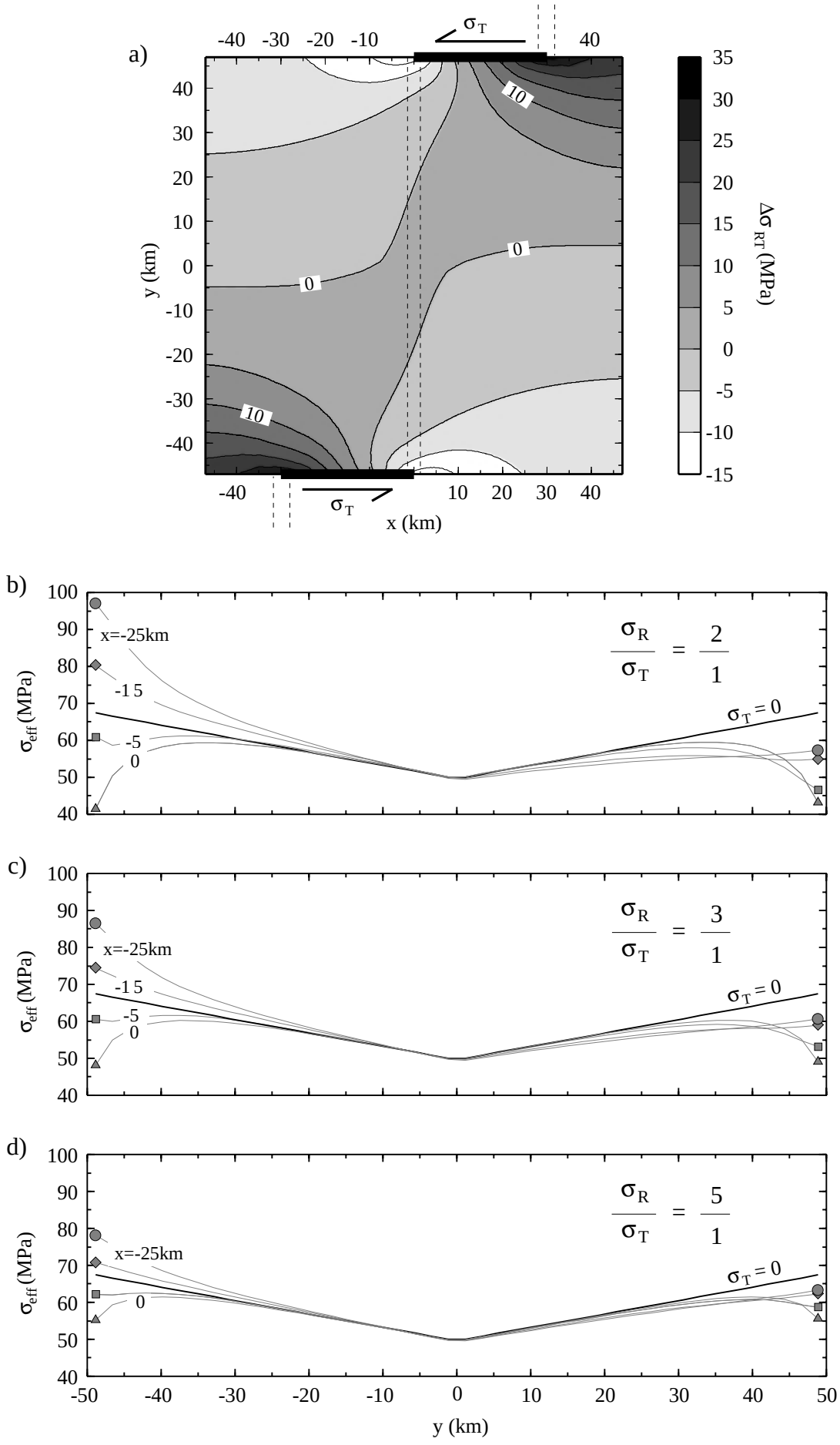
a)
σT
-40 -30 -20 -10
40
10
0
0
10
40 30 20 10 0 -10 -20 -30 -40
y (km)
-40
σT
10 20 30 40
x (km)
35 30 25 20 15 10 5 0 -5 -10 -15
ΔσRT (MPa)
b)
σR/σT = 2/1
x=-25km
-15
-5
0
σT = 0
σeff (MPa)
c)
σR/σT = 3/1
x=-25km
-15
-5
0
σT = 0
σeff (MPa)
d)
σR/σT = 5/1
x=-25km
0
σT = 0
σeff (MPa)
100 90 80 70 60 50 40
-50 -40 -30 -20 -10 0 10 20 30 40 50
y (km)

Figure 12